This is a preprint, the final version is subject to change, of the American Mineralogist (MSA)
Cite as Authors (Year) Title. American Mineralogist, in press.
DOI: https://doi.org/10.2138/am-2018-6258

Revision 1

Combined Fe-Mg chemical and isotopic zoning in olivine constraining magma mixing-to-eruption timescales for the continental arc volcano Irazú (Costa Rica) and Cr diffusion in olivine

Martin Oeser [1,*], Philipp Ruprecht [2,3], and Stefan Weyer [1]

[1] Leibniz Universität Hannover, Institut für Mineralogie, Callinstr. 3, 30167 Hannover, Germany

[2] University of Nevada, Department of Geological Sciences, 1664 N. Virginia Street, Reno, NV 89557, USA.

[3] Columbia University, Lamont-Doherty Earth Observatory, 61 Route 9W, Palisades, NY, USA

[*] corresponding author

email addresses:

Martin Oeser: m.oeser@mineralogie.uni-hannover.de

Philipp Ruprecht: pruprecht@unr.edu

Stefan Weyer: s.weyer@mineralogie.uni-hannover.de

This is a preprint, the final version is subject to change, of the American Mineralogist (MSA)
Cite as Authors (Year) Title. American Mineralogist, in press.
DOI: https://doi.org/10.2138/am-2018-6258

Abstract

Arc magmas commonly are mixtures of newly-arriving primitive melts, stored magmas at shallow levels, and xenolithic material added on ascent. Almost every eruption has a unique assembly of these components, which may record magmatic processes occurring in the plumbing system prior to an eruption. In this study, we focus on complexly zoned olivines (crustal xenocrysts) in order to obtain a better understanding of the magmatic processes and the assembly of the 1963-65 erupted magmas of Irazú volcano, one of the most voluminous active volcanoes in Costa Rica. We performed high-precision in-situ Fe-Mg isotope analyses by femtosecond-LA-MC-ICP-MS on these olivines, in order to unravel the origin of their complex chemical zoning (growth, diffusion, or a combination of both processes). This information was used to establish a refined diffusion model to explore magma mixing-to-eruption timescales. Furthermore, trace element analyses using LA-ICP-MS were performed. Chromium displays a chemical zoning in the investigated olivine, which coincides spatially as well as in terms of length scale and geometry with Fe-Mg zoning and which was used to constrain Cr diffusivity in natural olivine.

Our findings show that Fe-Mg zoning in Irazú olivine mainly results from Fe-Mg inter-diffusion after two crystal growth episodes as indicated by strongly coupled chemical and isotopic zoning. Simulations of this diffusive process indicate that mixing of these crystals into ascending primitive melts occurred <600 days before their eruption, consistent with a previously reported diffusion study based on Ni zonation in Mg-rich olivines. Trace element characteristics of olivine suggest that the complex-zoned olivine crystals originate from a crystal mush/cumulate in the middle or lower crust and deeper than the shallow magma chamber and were mobilized by mantle-derived magma bearing Mg-rich olivines. Finally, modeling of the observed Cr zoning in the Irazú olivines indicates that the diffusion coefficient for Cr in olivine (D_{Cr}) is smaller than $D_{Fe\text{-}Mg}$ by a factor of

4.9 ± 2.9 at the conditions experienced by these crystals consistent with Cr diffusion experiments at high silica activity in the melt.

Our results show that by combining elemental and isotope zoning studies in individual minerals we can refine the timing/assembly of magmatic eruptions and provide independent constraints on element diffusivities. Lastly, it confirms that primitive arc magmas at Irazú are not aphyric during ascent, but carry primitive phenocrysts from lower crust or Moho depth to the surface.

Keywords: olivine; Fe-Mg zoning; stable isotopes; laser ablation; diffusion modeling; Cr diffusivity; magma assembly

Introduction

Intermediate arc magmas frequently contain diverse crystal populations, many of which are not in equilibrium with the host melt. As a result many crystals re-equilibrate with their host melt, either through chemical diffusion, crystallization/dissolution or a combination of these processes. Snapshots of these transient processes, such as chemical zoning in crystals, are frozen at the time of eruption when magmas cool down rapidly. If diffusion is the dominant process to achieve equilibrium between crystal and melt, the chemical zoning can be used to obtain time information about the evolution of magmatic systems by diffusion modeling, provided that diffusion rates of elements in the minerals of interest are known. The diffusion of Fe and Mg in olivine has been intensely investigated in experimental studies for more than 30 years (reviewed by Chakraborty 2010), and several studies have used Fe-Mg chemical gradients in magmatic olivine crystals in order to estimate timescales of magma evolution processes by diffusion modeling (e.g. Costa and

Chakraborty 2004; Costa and Dungan 2005; Kahl et al. 2011; Kahl et al. 2013; Hartley et al. 2016; Rae et al. 2016), relying on the parameterization for the Fe-Mg inter-diffusion coefficient given by Chakraborty (1997) and Dohmen and Chakraborty (2007). However, as crystal growth and elemental diffusion often show similar zoning patterns it remains questionable whether calculated diffusion timescales represent the timing of a specific magmatic process (Shea et al. 2015). As shown in recent studies, combining the information of Fe-Mg chemical variations and in-situ analyses of Fe-Mg stable isotope ratios in olivine represents a powerful means to elucidate diffusion and/or growth/dissolution processes (Sio et al. 2013; Oeser et al. 2015). As diffusion generates large kinetic isotope fractionations (e.g. Richter et al. 2003) diffusion-generated chemical zoning is coupled with pronounced isotopic zoning, in contrast to chemical zoning that developed in absence of diffusion (Oeser et al. 2015). Detailed chemical and isotopic profiles across magmatic olivines may thus be used to unravel complex crystal growth- and diffusion histories, which are indistinctly recorded by chemical zoning alone (e.g. Collinet et al. 2017; Sio and Dauphas 2017).

In this study, we aim to investigate the magmatic events recorded in complexly zoned olivine crystals in basaltic andesites of the 1963-65 eruption of the Irazú volcano, one of the most voluminous (e.g. Carr 1984) and active volcanoes in Costa Rica, with recurring explosive andesitic eruptions potentially endangering ~1.6 million people living within 30 km of this stratovolcano (Global Volcanism Program 2013). Previously, investigation of Ni zoning in primitive (magnesian) olivines from this eruption suggested that magma transport from the Moho to the surface occurred on timescales comparable to the duration of the eruption (~2 years), thus indicating that the eruption was likely fed (and triggered) by magmas extracted from the mantle (Ruprecht and Plank 2013). This study provides a more comprehensive picture of the pre-eruptive mixing and assembling of erupted 1963-65 magmas, focusing on complexly zoned (in terms of Fo contents)

olivines. These crystals share the normal zoning history of the rims of the mantle-derived magnesian olivines. By unraveling the origin of their complex zoning we establish the basis for appropriate diffusion modeling. This will eventually yield reliable mixing-to-eruption timescales and provide a more detailed picture of the complex history of these crystals, leading to a better understanding of the magmatic processes and the assembly of the erupted magmas beneath Irazú volcano.

Moreover, through the refinement of timescale estimates using in-situ isotope records we can also assess the diffusivity of slow-diffusing elements, for which experimental studies are challenging (e.g. Milman-Barris et al. 2008). Natural samples have been used elsewhere (e.g. Mallmann et al. 2009; Qian et al. 2010; Tollan et al. 2015) to compare results to experimentally determined diffusion coefficients (e.g. Ito and Ganguly 2006; Spandler and O'Neill 2010; Zhukova et al. 2017; Jollands et al. 2014, 2018). Notably, Cr diffusivities display a large range in the literature (Ito and Ganguly 2006; Milman-Barris et al. 2008; Spandler and O'Neill 2010; Jollands et al. 2018). The recent study of Jollands et al. (2018) suggested that this large range is a result of variations in SiO_2 activity (a_{SiO2}), an effect that has also been recognized for other trace elements in olivine (Jollands et al. 2014, 2016a; Zhukova et al. 2014). Independent timescale estimates (specifically more robust by combining elemental and isotopic zoning) can also be used to constrain diffusivities of such slow-diffusing elements and help to provide additional constraints to reconcile variations in experimentally determined diffusivities. The complexly zoned olivine crystals in basalts of the 1963-65 eruption that are close to the SiO_2 activity buffer of olivine-enstatite are suitable for such an approach since Fe-Mg zoning coincides with Cr zoning (and to a lesser extent also V and Al zoning).

The Irazú magma system and samples

The Irazú magmatic plumbing system has been characterized geophysically and geochemically (Alvarado et al. 2006; Dzierma et al. 2010; Ruprecht and Plank 2013). Seismic studies highlight a low-velocity region in the upper crust (5-10 km) commonly interpreted to represent the major magma storage region. Furthermore, the Moho depth has been constrained seismically to ~35-45 km (Lizarralde et al. 2010; Gazel et al. 2015).

Geochemical constraints emphasize the hybrid nature of Irazú magmas, particularly the 1963-65 eruption (Alvarado et al. 2006). Whole-rock compositions represent mixtures of basaltic and dacitic end-members. While geophysics and whole-rock geochemistry provide a simplified view of the magma plumbing system, more detail is recorded within the crystal cargo. Firstly, crystals from individual samples show a large compositional diversity that mimics the whole rock end members (An40-80, Fo72-91; Alvarado et al. 2006; Ruprecht and Plank 2013). However, a detailed look into the crystal cargo reveals that it is inadequate to explain the complex crystal cargo with mantle-derived magmas that simply rise to the shallow region where they differentiate and hybridize. In this study we focus on olivine crystals (with xenocrystic cores; see below) that provide a unique view into the magma assembly from the mantle to the surface. Ruprecht and Plank (2013) reported on the major and trace element geochemical diversity in olivines from the 1963-65 eruption. Based on their results, at least three different olivine types in the Irazú eruption can be distinguished: 1) magnesian olivines (Fo_{89-91}) which were the focus of Ruprecht and Plank (2013), type A; 2) complex olivines that show significant reversals in their Fo contents and are the focus of this study, type B; and 3) intermediate to low Fo olivines at low Ni content that represent shallow crustal processes of fractionation and mixing (type C; Fig. 1). It is notable here, that these three types of olivines represent end-member compositions, and the full olivine population shows crystals that are intermediate between those end-members. Potentially, the “reservoirs” that are represented by the

three olivine end-members have either some internal variation, e.g., due to incomplete mixing (Ruprecht et al. 2008; Schleicher and Bergantz 2017) resulting in a range in composition, or they are partially open to interact with each other beyond just the processes directly driving the 1963-65 eruption. In the "Results" section we are going to describe in greater detail the type B olivines, which are the main focus of this study. The samples analyzed herein (IZ-10-11/-12/-13) comprise crater rim deposits of the 1963-65 eruption on the SW side of the major Irazú crater which are juvenile scoria-rich tephra and fine lapilli tephra (Ruprecht and Plank 2013). From these samples, we investigated 10 olivine crystals (three of type A, seven of type B) for their major and trace elements characteristics and their Fe- and Mg isotopic compositions by microanalytical techniques (see next section).

Methods

In-situ major and trace element analyses of olivines

Major and trace element laser ablation data were analyzed using a VG PQ ExCell and NewWave 196 nm ArF Eximer laser at Lamont-Doherty Earth Observatory during the study of Ruprecht and Plank (2013). The data acquisition was done in line mode and the continuous time series data was then processed into individual data points by combining a finite number of steps. Each sweep from Li-7 to Y-89 took 0.36 s, with dwell times of 10 ms on each mass (for all masses analyzed see Table S1). The raw data was processed following standard calibration techniques for LA-ICPMS (using a Matlab code developed by P. Ruprecht), but using Fe and Mg count rates and olivine stoichiometry to calculate the internal standard concentration of MgO. Comparisons with microprobe profiles show that for magnesian olivines this procedure produces Fo contents within 0.5 mol units of electron microprobe results (Ruprecht and Plank 2013). San Carlos olivine San

Carlos USNM 1113142/44 was used to normalize results from different days and to assess the measurement uncertainties. While this procedure may introduce a small systematic difference to other datasets in the literature related to potentially small heterogeneities in San Carlos trace element abundances across labs, it ensures that analyses are internally comparable. The concentrations used for San Carlos olivine were reported in Ruprecht and Plank (2013) and recalculation to other standards is trivial. A more detailed San Carlos olivine study is underway, but it is not the scope if this paper. The combined data points are recorded for every 5.8 μm, which is less than the spot size of the laser (25 μm) and therefore does not represent the true spatial resolution of the analysis. Given the continuous movement across the sample (3 μm/s), some smearing of the signal will occur and the spatial resolution is therefore similar to the laser spot size (Bradshaw and Kent 2017). Recently we recognized that in our instrument Ca concentration data are affected by interference of ^{28}Si and ^{16}O on mass 44, thus the Ca data needs to be interpreted cautiously. We focus here on inferred Fo content as well as the cations V, Cr, and Al. Al counts were statistically indistinguishable from the background for one sample (IZ-10-13), which was measured on a different day than IZ-10-12, which was measured during a day of better instrument sensitivity. LA-ICP-MS results of the olivines investigated in this study can be found in the supplementary material (Table S1). Olivines were repolished after these LA-ICP-MS analyses in order to determine crystal orientations by electron backscatter diffraction (see below) and to acquire BSE images.

In-situ Fe and Mg isotope analyses of zoned olivines

Profiles of Fe and Mg isotopic compositions in zoned olivines were acquired in-situ by femtosecond-laser ablation-MC-ICP-MS (fs-LA-MC-ICP-MS) at the Institut für Mineralogie of the Leibniz Universität Hannover, following the analytical procedures described in Oeser et al. (2014)

and Oeser et al. (2015). In summary, a Spectra-Physics Solstice fs-LA system is coupled to a Thermo-Finnigan Neptune Plus MC-ICP-MS, which is operated in high mass resolution mode in order to resolve molecular interferences of argon nitrides and argon oxides on Fe isotopes and isobaric interferences (e.g. $^{52}Cr^{2+}$) on Mg isotopes. Laser repetition rate was between 30 Hz and 70 Hz during Fe isotope analyses and between 20 Hz and 45 Hz during Mg isotope analyses, depending on the Fe and Mg concentrations in the ablated material. Fluence of the fs-LA system in Hannover is on the order of 1 J/cm². Further details of the fs-LA system can be found in Oeser et al. (2014) and Lazarov and Horn (2015). The instrumental mass discrimination of the MC-ICP-MS was monitored during Fe isotope ratio determination by simultaneously analyzing the Ni isotope ratios of a Ni reference solution (NIST SRM 986) combined with a sample-standard bracketing protocol. For Mg isotope analyses, only the sample-standard bracketing technique was used to correct for drifts of the instrumental mass bias. With this analytical procedure, the LA analyses yield a long-term reproducibility of ±0.13‰ (2 SD) for both $\delta^{56}Fe$ and $\delta^{26}Mg$, based on replicate analyses of silicate reference glasses (e.g. BHVO-2G, ML3B-G) over a period of three years. During a single analytical session (1-2 days) the reproducibility of $\delta^{56}Fe$ and $\delta^{26}Mg$ values for the reference glasses is always better than ±0.10‰ (2 SD). The LA analyses on olivines from Irazú were guided by previously acquired BSE images (Ruprecht and Plank 2013). Sample material was ablated with a laser spot size of 35-40 µm (in diameter) by line scans either (i) parallel to the crystal rim (i.e. parallel to the chemical zoning; Fig. 2a and 2b) with a laser scan speed of 20 µm/s and a cycle integration time of ~1 s or (ii) perpendicular to it with a laser scan speed of 2-3 µm/s and a cycle integration time of ~0.5 s (Fig. 2c and 2d). The latter technique was applied if the exposed area on the crystal was not sufficient to perform line scans (with sizes of ~150x40 µm) parallel to the chemical zoning. In case (i), one ablation line yields one δ-value. In case (ii), the mean of 15-20 individual ratio measurements is used to calculate one δ-value. As a consequence,

the precision (2σ) of a single δ-value determined in such a way is usually not as high as for case (i), i.e. better than ±0.10‰, but still better than the long-term reproducibility of ±0.13‰. For case (ii), 2σ is calculated by propagating the errors (SE) of the bracketing standards (n ≈ 120 cycles) and of the analyzed sample (n = 15-20 cycles), as follows:

$$2\sigma = 2 \times 1000 \times \left[\left(\frac{SE_{\text{std1}}}{R_{\text{std1}}}\right)^2 + \left(\frac{SE_{\text{std2}}}{R_{\text{std2}}}\right)^2 + \left(\frac{SE_{\text{sample}}}{R_{\text{sample}}}\right)^2\right]^{0.5} \quad (1)$$

where R is either $^{56}Fe/^{54}Fe$ or $^{26}Mg/^{24}Mg$.

Electron microprobe and electron-backscattered diffraction analyses

After the in-situ isotope ratio analyses by fs-LA-MC-ICP-MS, all olivine crystals were carefully repolished, thus removing a layer of ~10 µm in thickness. Because the laser ablation lines have approximately a Gaussian shape (in cross-section; Fig. S1 and S2 in the supplementary material), this repolishing decreased the sizes of the LA lines significantly, enabling us to determine major and minor element concentrations by electron micropobe analyses (EMPA) very close to the isotopic profiles.

A Cameca SX-100 with 5-wavelength dispersive spectrometers at the American Museum of Natural History in New York was used for post-isotope analysis electron microprobe work. Analyzes were performed utilizing a focused beam (1 µm diameter), 20 nA beam current, and 15 kV accelerating voltage. The instrument was calibrated on forsterite (Mg (30 s, peak counting times), TAP (analyzer crystal)), plagioclase (Al (60 s), TAP), clinopyroxene (Si (30 s), TAP; Ca (80 s), PET), magnesiochromite (Cr (40 s), LPET), rhodonite (Mn (40 s), LPET), fayalite (Fe (30 s), LLIF), and Ni-diopside (Ni (60 s), LLIF). Reference olivines San Carlos and Ol174.1 (n=5 each) were measured together with unknowns. We estimate the reproducibility from the repeat measurements of reference olivines to be within ~2 % (2SD relative), <5%, <20%, and <50% for

major elements, Ni, Mn, and Ca, respectively. Calculated Mg# for San Carlos (89.79 ± 0.09, 2SD absolute) and Ol174.1 (90.24 ± 0.33) are within error of published values (White 1966; Jarosewich et al. 1980). Cr and Al in reference materials were below the detection limits for this analytical protocol (~200 ppm), but analyzed to identify mixed analyses with spinel. A complete table of quantitative electron microprobe analyses together with BSE images can be found in the supplementary material (Table S2).

To account for diffusive anisotropy crystal lattice orientations relative to the 1D-zoning traverses were determined via electron-backscattered diffraction (EBSD). EBSD measurements were performed as part of the analytical session reported in Ruprecht and Plank (2013). A Zeiss Supra 40VP scanning electron microscope, Oxford energy-dispersive X-ray spectroscopy and HKL electron back-scatter diffraction (EBSD) integrated system was used at the Marine Biological Laboratory in Woods Hole. Diffraction patterns were matched against a reference olivine lattice model and Euler angles were recorded for a rotation from the reference frame to the observed orientation. Rotation information is provided in the supplementary material (Table S3).

Results

As described above, the Irazú 1963-65 samples investigated by Ruprecht and Plank (2013) and in this study contain principally three different olivine types. We define type B olivines as large crystals (>500 μm) with intermediate Fo core (Fo_{80-87}). Reverse zoning from the core to the mantle of the crystals links the crystallization history of type A and type B olivines (Fig. 1). The high Fo mantles never reach the most magnesian compositions recorded in type A olivines, but join the normal zonation near the rim at ~ Fo_{87} to $Fo_{90.5}$. The mantle zoning of major elements in type A and B is correlated with the same zoning features in minor and trace elements (e.g. Ni, Cr, Al, V;

Fig. 3). In contrast, the cores of these two types are significantly different also in trace element inventory (Fig. 4). Exemplary for this difference are the elevated Ni and low Cr concentrations, a trace element signature that is consistent with a xenocrystic origin for the type B cores. Such signatures are commonly associated with olivine cumulates (e.g. Otamendi et al. 2016), where partitioning and diffusive exchange of Ni and Cr leads to a preferential incorporation in olivine and pyroxenes, respectively.

Given the zoning characteristics of the different olivines in the 1963-65 eruption, exploring their relative contributions to individual samples shows that the crystal cargo changed as the eruption progressed. We have only investigated three samples (IZ-10-11/-12/-13) that represent early, middle, and late stages of the eruption (see Ruprecht and Plank, 2013, for the sampling levels and further sample details). Some coexisting lavas also were investigated petrographically (samples from Benjamin et al. 2007), but have not been investigated as detailed as the tephra samples. While all samples contain type A and C olivines at fractions in significant quantities, type B olivines are rare in the early sample (IZ-10-11).

More specifically, the seven complexly zoned olivine crystals from Irazú volcano investigated in this study show reversely zoned ferrous cores (Fo_{80-87} to Fo_{87-90}, Fig. 5, Fig. S3), likely indicating (at least) two episodes of crystal growth. The rims of these crystals are always normally zoned (Fo_{87-90} to Fo_{79-84}, Fig. 5). Hence, as mentioned above, they appear to share the history of the rims of primitive magnesian olivines in the samples of the 1963-65 eruption of Irazú volcano. This normal chemical zoning at the rims may indicate either (i) crystal growth during fractional crystallization of olivine and clinopyroxene (and thus an evolution of the melt to higher Fe-Mg ratios) or (ii) diffusion of Fe into and Mg out of olivine driven by a compositional contrast between olivine and melt or (iii) a combination of both processes. As shown in previous studies, Fe-Mg isotopic profiles in such chemically zoned olivines can unravel which of the three possibilities is

the most likely one (Sio et al. 2013; Oeser et al. 2015; Richter et al. 2016; Sio and Dauphas 2017). Other means to distinguish between growth- and diffusion-generated zoning in a crystal include, for example, the investigation (i) of zoning profile lengths of various elements with different known diffusivities (e.g. Costa and Dungan 2005), and (ii) of the width of the chemical zoning in different crystallographic directions expected from diffusion anisotropy (e.g. Costa et al. 2008). Three solely normally zoned (Mg-rich) olivine crystals investigated in this study show more or less homogeneous cores (Fo_{88-90}) and strongly zoned rims (Fo_{88} to Fo_{78-80}, Fig. 6). One of these olivines (IZ-10-13 ol22) additionally shows reverse Ni zoning in its core, which has already been investigated by Ruprecht and Plank (2013).

Our in-situ Fe-Mg isotope data reveal a strong coupling of Fe-Mg chemical and isotopic zoning for all investigated olivines (Fig. 5 and 6, Fig. S3), along with largely negative correlations between $\delta^{26}Mg$ and $\delta^{56}Fe$ values (Fig. 7), indicating that Fe-Mg inter-diffusion is the dominant process responsible for the re-equilibration of these olivines (cf. Teng et al. 2011; Sio et al. 2013; Oeser et al. 2015). A few Mg isotope data points clearly deviate from the overall negative correlations between $\delta^{26}Mg$ and $\delta^{56}Fe$ values (Fig. 7). The origin of these "outliers" is unknown, but may be related to the fact that Mg and Fe isotope profiles for a certain olivine cannot be measured at the exact same positions in the crystal (see Fig. 2). Nevertheless, in these relatively Mg-rich olivines (Fo contents vary between 78 and 90 mol%), Fe isotope variations are much more pronounced than Mg isotope variations (Fig. 7), for mass balance reasons, and thus can put tighter constraints on the history of these crystals (see section "Discussion"). As a consequence, we will focus on Fe isotopic zoning, in combination with Fe-Mg chemical zoning, in the following sections. However, in the supplementary material we also show modeling results for Mg isotopic zoning in some olivine crystals (Fig. S4).

The olivines investigated here for Fe-Mg isotopes have a distinct trace element characteristic. In particular, the olivines with intermediate Fo, high Ni cores overgrown by high Fo, high Ni rims have unique Cr concentrations among all 1963-65 Irazú olivines. The cores have low Cr concentrations in a few crystals less than 10 ppm (Fig. 3), which is uncommon for primitive magmatic olivine phenocrysts, and stands in contrast to the high Ni content for the given Fo content. On the other hand, the high Fo rims have Cr contents that are more common in primitive arc olivines >100 ppm. This extreme difference between those cores and the rims and any other primitive Irazú olivine is best expressed in the Ni/Cr ratio, which for normal olivines ranges between 10 and 15, but reaches 370 in some cores of the intermediate Fo, high Ni olivines (Fig. 4). In addition to the unique Ni/Cr ratios, the zoning of trace elements generally correlates with major element zoning and therefore can potentially be linked to the timescales obtained here via the Fe-Mg isotopes and Fe-Mg elemental zoning. We note that many trace elements have zoning that correlates with major element zoning, however, we focus here solely on Cr, V, and Al zoning, because these have received particular attention given the recent controversy about their diffusivities in olivine (Ito and Ganguly 2006; Spandler et al. 2007; Milman-Barris et al. 2008; Spandler and O'Neill 2010). For all crystals that have zoning of Cr, V, and Al, the lengthscales of the zoning are shorter than the Fe-Mg zoning, however of a similar order of magnitude.

Diffusion modeling

The simulation of observed Fe-Mg chemical and isotopic zoning in Irazú olivines by diffusion modeling generally follows the approaches presented in Oeser et al. (2015). In particular, in order to reproduce the reverse zoning of the complexly zoned olivines (hereafter referred to as diffusion episode 1) two models were applied: the first one comprises the internal homogenization of an

olivine by Fe-Mg inter-diffusion after two growth episodes which generate a step function in the Fo content profile (magnesian rim, ferrous core) but homogeneous Fe and Mg isotopic compositions (scenario 3 in Oeser et al. 2015). For this case, we assumed a plane sheet geometry and solved the following one-dimensional expression of the diffusion equation numerically by the method of finite differences (e.g. Crank 1975; Costa et al. 2008):

$$\frac{\partial C_{\mathrm{i}}(x,t)}{\partial t} = \frac{\partial}{\partial x}\left[D_{\mathrm{i}}\frac{\partial C_{\mathrm{i}}(x,t)}{\partial x}\right] \quad (2)$$

where C_{i} is the concentration of element i, t is time, D_{i} is the diffusion coefficient of element i, and x is distance. The second possible model encompasses the growth of a Mg-rich rim around a homogeneous ferrous olivine crystal, but now associated with simultaneous Fe-Mg inter-diffusion (scenario 4 in Oeser et al. 2015). Here, the olivine is assumed to be a semi-infinite medium, and we use the same analytical solution to this moving boundary problem as given in Oeser et al. (2015):

$$C(x,t) = C_0 + (C_{\mathrm{rim}} - C_0) \times \exp\left[\frac{R\left(x-\frac{Rt}{2}\right)}{2D}\right]\frac{1}{2}\exp(\lambda t)\left\{\exp\left(-x\sqrt{\frac{\lambda}{D}}\right)\mathrm{erfc}\left[\frac{x}{2\sqrt{Dt}} - \sqrt{\lambda t}\right] + \exp\left(x\sqrt{\frac{\lambda}{D}}\right)\mathrm{erfc}\left[\frac{x}{2\sqrt{Dt}} + \sqrt{\lambda t}\right]\right\} \quad (3)$$

where C_0 is the initial concentration of the element of interest (as measured in the core of the olivine crystal), C_{rim} is the concentration of this element in the overgrowing rim, t is time, D is the diffusion coefficient, R is the growth rate, $\lambda = R^2/(4D)$, and x is distance.

Simple Fe-Mg exchange between olivine and melt (scenario 1 in Oeser et al. 2015) was modeled by applying a fixed rim composition and Fe-Mg inter-diffusion in olivine with a plane sheet geometry. In this case, the diffusion equation (eqn. 2) was solved numerically by the method of finite differences. This model was used to reproduce the normal zoning at the rims of the investigated olivines from Irazú volcano (hereafter referred to as diffusion episode 2). Further

initial and boundary conditions are given in the following paragraph and in section "Diffusion episode 1".

According to the parameterization given by Dohmen and Chakraborty (2007), which we applied in this study, the diffusion coefficient for Fe-Mg diffusion in olivine depends on oxygen fugacity (fO_2), the mole fraction of the fayalite component (X_{Fe}), pressure (P), temperature (T), and the crystallographic orientation, i.e. the orientation of each measured profile relative to the crystallographic axes determined by electron backscatter diffraction. The latter was used to calculate the diffusion coefficient for individual profiles, following the approach given in, e.g., Costa and Chakraborty (2004). The presence of water in an olivine crystal can also significantly affect $D_{Fe\text{-}Mg}$ in olivine (Wang et al. 2004; Hier-Majumder et al. 2005). We have not investigated whether the Irazú olivines contain significant amounts of water (i.e. >11 ppm, as reviewed by Chakraborty 2010), and thus we do not account for effects from hydrogen. However, Irazú magmas commonly contain ~ 3 wt% H_2O (Benjamin et al. 2007) and coexisting olivines may contain therefore significant amounts of water. Thus, our modeled timescales represent maximum estimates, as the presence of H^+ in olivine increases $D_{Fe\text{-}Mg}$ by up to one order of magnitude relative to anhydrous conditions (e.g. Jollands et al. 2016b). The durations of the diffusive processes were estimated at isothermal conditions, and temperature estimations in this study rely on thermometry data for Irazú magmas presented in Alvarado et al. (2006), Benjamin et al. (2007) and Ruprecht and Plank (2013). In particular, for diffusion episode 1 we assumed a temperature of 1150°C, consistent with the temperature range (1100-1200°C) used for simulating Ni diffusion profiles in the magnesian olivines from Irazú (Ruprecht and Plank 2013). For the second diffusion episode, a temperature of 1080°C was used for diffusion modeling, consistent with temperature estimations based on whole rocks and melt inclusions of more evolved compositions (Benjamin et el. 2007), as

this diffusion event likely occurred in the plumbing system in the shallow crust (see below). The oxygen fugacity was assumed to be $\Delta\log fO_2$ (NNO) = +1 (Benjamin et al. 2007), and its absolute value at the given temperature was calculated following the parameterization of Schwab and Küstner (1981). As the compositional variability concerning X_{Fe} is rather limited, i.e. fayalite contents range from 0.22 to 0.12 for the investigated olivines, X_{Fe} was presumed to be constant at an average value of 0.15 in all simulations. The uncertainty introduced by this simplification on $D_{Fe\text{-}Mg}$ (and, hence, on the calculated timescales) is smaller than a factor of 1.6. Pressure variations have the least effect on $D_{Fe\text{-}Mg}$, compared to variations in T, fO_2, X_{Fe}, or orientation, and given the pressure range experienced by the investigated olivine crystals (~0.1-500 MPa). Following the pressure estimation made for the magnesian Irazú olivines (Ruprecht and Plank 2013) we assumed P to be 500 MPa and 100 MPa during diffusion episode 1 and 2, respectively.

The (kinetic) isotope fractionation associated with the Fe-Mg inter-diffusion was modeled by applying the following empirical formula (e.g. Richter et al. 1999):

$$\frac{D_q}{D_r} = \left(\frac{M_r}{M_q}\right)^{\beta} \qquad (4)$$

where D represents the diffusion coefficient, q and r are isotopes of a certain element (e.g., ^{54}Fe and ^{56}Fe), and M is the atomic mass in a.m.u. The exponent β is an empirical constant and equal to 0.5 in ideal monoatomic gases (Van Orman and Krawczynski 2015). For olivine, β-values appear to depend on crystal composition and diffusion direction relative to the orientation of the crystallographic axes (Van Orman and Krawczynski 2015) and, as the systematics of these dependencies is not clear yet, they are thus difficult to predict; however, they can be estimated by fitting observed isotope diffusion profiles across (natural) olivine crystals. Studies by Sio et al. (2013), Oeser et al. (2015) and Richter et al. (2016) indicate that β-values for olivine fall in a range

of 0.055-0.16 for Mg and of 0.075-0.30 for Fe. In this study, Fe and Mg isotopic profiles were fitted by adjusting the respective β-values, i.e. modifying the diffusivity ratio of two isotopes of the same element (e.g. ^{54}Fe and ^{56}Fe) until the amplitude of the modeled isotope fractionation matched that of the observed one. As a consequence, the used β-values are purely empirical and characteristic for the given simulated case. In this study, β_{Fe}-values used range from 0.12 to 0.25 (Table 1), and therefore fully agree with previous estimates of β_{Fe} in olivine (Sio et al. 2013; Oeser et al. 2015; Collinet et al. 2017).

Discussion

Sequence of events recorded by complexly and normally zoned Irazú olivines

The zoning characteristics of type B olivines provide unique constraints on the spatial origin of these crystals and the temporal incorporation of different end-members into the eruption. As type A and type B crystals have a shared history within the outer zones of the crystals and type B olivines merge onto the general geochemical evolution recorded in type A olivines we suggest that the xenocrystic type B cores were remobilized in the crust by ascending mantle-derived melts carrying the magnesian type A olivines. This is evidence that the mixing event recorded by Ni zonation in magnesian type A olivines occurred at deeper levels than the storage depth of the xenocrystic type B olivines (which is likely to be >15 km beneath the volcano's summit based on the trace element characteristics of type B olivines; see below), further corroborating the assumption of near-Moho origin of the primitive type A olivines (Ruprecht and Plank, 2013). In addition to the compositional differences, type B complex olivines are also not uniformily distributed within the 1963-65 eruption. Of the three samples studied in the past, IZ-10-11 (the earliest phase of the eruption

418 studied by Ruprecht and Plank, 2013) lacks significant amounts of type B olivines, while type A
419 and C are both common. Type B olivines are most common in IZ-10-12, but also present in IZ-10-
420 13, suggesting that the assembly of the 1963-65 eruption is complex where some components wane
421 and wax.
422 The complex zoning of the Irazú type B olivines investigated in this study points to at least two
423 episodes of crystal growth under diverse crystal-melt equilibrium conditions. The intermediate Fo
424 contents (Fo_{80-87}), high Ni concentrations (2600-3200 ppm Ni), and anomalously high Ni-Cr ratios
425 (Fig. 4) in the cores of these olivines indicate that these crystals were formed and equilibrated in
426 the middle or lower crust beneath Irazú volcano, probably in a crystal mush or mafic cumulate (see
427 section "Assembling the Irazú magma"). The Mg-rich zone near the rims of the complexly zoned
428 olivines may then have formed by crystal growth when these crystals were entrained into ascending
429 mantle melts and brought into the plumbing system in the shallow crust beneath Irazú volcano. The
430 sharp intra-mineral chemical gradient produced by this second growth event was eventually
431 smoothed out by Fe-Mg inter-diffusion as implied by the strong coupling of Fe-Mg chemical and
432 isotopic zoning. Modeling this diffusive process (diffusion episode 1) therefore yields information
433 about the time span from the entrainment of these olivines in the crust to the eruption. Previous
434 studies have used similar Fe-Mg zoning patterns (initial step function, subsequent diffusive
435 relaxation) in olivine to estimate mixing-to-eruption timescales by diffusion modeling (e.g. Kahl et
436 al. 2011, 2013; Longpré et al. 2014; Hartley et al. 2016). However, all of these studies assumed
437 that the observed zoning was the result of instantaneous growth of a crystal layer with a different
438 composition than the core and subsequent Fe-Mg inter-diffusion (cf. scenario 3 in Oeser et al.
439 2015), which provides maximum timescales. In this study, we additionally apply a model where
440 crystal growth and Fe-Mg inter-diffusion occur simultaneously (scenario 4 in Oeser et al. 2015). As
441 shown in Oeser et al. (2015), Fe-Mg isotopic profiles as obtained in this study can provide a further

442 constraint which one of the two scenarios is more appropriate to describe the history recorded by
443 intra-mineral zoning of olivine, leading to more reliable timescales obtained from diffusion
444 modeling.
445 The similar zoning patterns at the rims of the complexly zoned olivines and of the primitive
446 olivines ($Fo_{\sim 88}$ to $Fo_{\sim 80}$) from Irazú indicate that both crystal populations experienced a comparable
447 late-stage history prior to the eruption. This likely included mixing with resident evolved magmas
448 in the shallow crust as well as fractional crystallization from and, thus, further differentiation of the
449 hybrid melt. The relative enrichment of light Fe and heavy Mg isotopes in the normally zoned part
450 near the olivine rim implies that diffusive Fe-Mg exchange between crystal and melt represents the
451 main process for the re-equilibration of olivine during that stage. It has to be noted that in some
452 olivines the width of the normal zoning is so narrow that inversely correlated Fe-Mg isotopic
453 profile cannot unambiguously be resolved by the LA technique used in this study, given the spatial
454 resolution of 30-40 µm. However, olivines with wide normal zoning (e.g. IZ-10-13 ol22 and ol31
455 in Fig. 6 and Fig. S3, respectively) clearly show anti-correlated Fe-Mg isotopic profiles, which
456 strongly argues for a diffusion origin of the normal zoning. As a consequence, we interpret this
457 normal zoning to mainly be the result of a second diffusion episode (whose duration can be
458 estimated by diffusion modeling) occurring in the shallow crust (shortly) prior to eruption.
459
460 **Timescales of diffusion episodes**
461 **Diffusion episode 1.** As described above, we applied two models to simulate the reverse zoning of
462 the complexly zoned olivines (diffusion episode 1). The first one (instantaneous growth and
463 subsequent Fe-Mg inter-diffusion) provides maximum timescales for the diffusive process, while in
464 the second model (crystal growth and simultaneous Fe-Mg inter-diffusion) the shape of the
465 simulated profiles depends on the timescale, as well as on the ratio of crystal growth rate (R in m/s)

and diffusion coefficient of Fe-Mg diffusion in olivine (D in m^2/s; see Fig. S5 for further details). Since D is determined by the chosen model parameters (T, P, fO_2, etc.) and assumed to be identical in both models, the second model yields a timescale for the diffusive re-equilibration of the crystal and additionally the growth rate of the Mg-rich layer. Following the stepwise modeling approach presented in Kahl et al. (2011), the diffusion profiles generated during the first diffusion episode are used as the initial concentration (and isotopic) gradients for diffusion episode 2, which produced the normal zoning at the rims of the complexly zoned and primitive olivines investigated herein. Hence, the reverse zoning of diffusion episode 1 is not simulated to full completion, in order to allow for further relaxation during the second diffusion episode. The results of this diffusion modeling approach are shown in Tables 1 and 2, and representative simulated diffusion profiles for four complexly zoned olivines are illustrated in Figures 8 to 11. Our results indicate that the duration of diffusion episode 1 was between ~90 days and ~530 days (Table 1). These timescales imply that the transfer of material from the lower crust to the shallow plumbing system beneath an active volcano can occur in less than two years or even within a few months. This is consistent with observations made by Ruprecht and Plank (2013) for primitive magnesian olivines with reverse Ni zoning, which have been transported with mantle-derived magmas through the crust at an average rate of 50-80 meters per day. The fact that the complexly zoned olivines still record quite a range of timescales of diffusive re-equilibration (90-530 days) may indicate (i) that not all of them were transported with the same mantle-derived magma batch, and/or (ii) that they were picked up from various parts of the crust beneath Irazú volcano at different points in time. The latter possibility is supported by the fact that the cores of these olivines show a range of Fo compositions from Fo_{80} to Fo_{87}, along with some variability in Fe- and Mg isotopic compositions, suggesting slightly different equilibration environments. Nevertheless, six out of the seven complexly zoned olivines investigated herein record diffusion timescales of less than 300 days for

the first diffusion episode, and thus a rapid transport into the shallow crust after being entrained into ascending mantle melts. These timescales are even shorter by up to ~25% if we assume that the growth of the Mg-rich layer and the diffusive equilibration of this intra-mineral chemical gradient occurred simultaneously during diffusion episode 1 (Table 2). Coeval growth and diffusion could also explain slight offsets (within ~ 30 μm) of the profile step locations for different elements required to fit Fe-Mg, Cr, V, and Al zoning profiles (Fig. 14). Unfortunately, neither the elemental zoning nor the Fe(-Mg) isotopic profiles can unequivocally unravel which of the two scenarios is the more likely one for the investigated olivines, i.e. both models (instantaneous growth + subsequent diffusion vs. growth + simultaneous diffusion) yield equally good fits for the Fe isotopic profiles in most olivines (Fig. 10). Only for one crystal (IZ-10-12 ol29) the second model reproduces the Fe isotopic profile much better (Fig. 11). The fairly good fits, that are obtained if the first model (instantaneous growth + subsequent diffusion) is applied, indicate that assumptions made in previous studies for similar Fe-Mg chemical profiles in olivine (e.g. Kahl et al. 2011; Longpré et al. 2014; Hartley et al. 2016) are reasonable (see above). In other words, based on the observations of this study, potential simultaneous crystal growth and diffusion appears to play a minor role in modifying Fe-Mg chemical and isotopic gradients in olivine. Nevertheless, only the combination of in-situ Fe-Mg concentration and isotopic analyses in olivine is capable of unraveling such complex growth+diffusion histories.

As described above, our second model (growth + simultaneous diffusion) does not only provide a timescale for the diffusion process, but also a growth rate for the Mg-rich layer. Based on the diffusion profiles observed in this study, these growth rates range from 3×10^{-12} m/s to 2×10^{-11} m/s (Table 2). Compared to experimentally determined growth rates of olivines in basaltic melts (10^{-10}-10^{-7} m/s, Donaldson 1975; Jambon et al. 1992), such growth rates seem to be exceptionally low. However, in natural systems olivine growth rates of 10^{-11}-10^{-9} m/s appear to be more realistic

(Maaløe 2011; Watson et al. 2015), probably due to a smaller degree of supercooling prevailing under natural conditions (cf. Jambon et al. 1992), and/or due to a decrease in the degree of supersaturation with time in a natural magma reservoir (cf. Maaløe 2011), which is less pronounced in experimental studies because of the limited runtime of the experiments.

Diffusion episode 2. The second diffusion episode, which generated the normally zoned rims of the complexly zoned and the primitive olivines investigated herein, lasted between a few days and ~450 days (Tables 1 and 2). One olivine records an exceptionally long timescale of diffusive re-equilibration in the second diffusion stage (~1450 days, IZ-10-13 ol21). It has to be noted again that these timescales − as well as the timescales for diffusion episode 1 − likely represent maximum estimates since we assume that the observed normal zoning is purely diffusion-generated (as implied by the inversely correlated Fe-Mg isotopic profiles, Fig. 6) and that the investigated olivines do not contain significant amounts of H^+ (which would strongly enhance $D_{Fe\text{-}Mg}$; e.g. (Hier-Majumder et al. 2005). However, we cannot exclude that crystal growth during fractional crystallization and further differentiation of the melt also had some influence on the development of that normal zoning, especially near the surface where cooling and partial degassing drive crystallization more effectively. Unfortunately, the spatial resolution of the LA technique used in this study is not sufficient to resolve the extent of this influence. As a consequence, we prefer to provide conservative, i.e. maximum, estimates for the timescales of processes beneath Irazú volcano. The variability of observed diffusion times for diffusion episode 2 may be an indication of a complex plumbing system beneath Irazú volcano where various crystal populations are stored in diverse magma batches for a certain amount of time before eruption. Still, short diffusion timescales, i.e. <200 days, appear to prevail, implying that magma mixing events in the shallow crust and following eruptions take place within a matter of months, if not days.

538

539 **Mixing-to-eruption times and magma ascent rates.** The stepwise modeling approach applied in
540 this study (see above) also allows us to estimate the time spans between the entrainment of the
541 complexly zoned olivines into ascending mantle melts and the eruption (t_{total} in Tables 1 and 2).
542 These timescales range from ~100 days to ~1750 days, with short timescales of <600 days (n = 6)
543 being more common than longer ones (n = 1). Assuming that these crystals were picked up
544 somewhere in the middle crust, i.e. ~15 km beneath the volcano's summit, given a crustal thickness
545 of ~35 km (Dzierma et al. 2010), the average ascent rate of the magmas carrying these olivines
546 through the crust would be 25 meters per day. Again, this represents a conservative estimate as (i)
547 several olivines record mixing-to-eruption timescales much shorter than 600 days, and (ii) the
548 complexly zoned olivines may have been entrained into ascending mantle melts at greater depth,
549 i.e. >15 km beneath the volcano's summit (see above). Also, such rates are averages, while
550 transient transport rates are likely much faster (e.g. Rubin 1995). Nevertheless, an average ascent
551 rate of 25 m/day is largely consistent with magma ascent rates of 50-80 m/day determined by
552 Ruprecht and Plank (2013) based on diffusion modeling of reverse Ni zoning in magnesian olivines
553 from the same sample suite and using a temperature range of 1100 to 1200˚C.

554

555 **Uncertainties of the modeled timescales.** As illustrated in, e.g., Oeser et al. (2015) and Kahl et al.
556 (2015), uncertainties of timescales calculated by Fe-Mg diffusion modeling mainly result from the
557 uncertainty of temperature estimations. In our case, we chose a temperature of 1150°C for diffusion
558 episode 1 which is well within the range of reported pre-eruptive temperatures of basalts from
559 Irazú volcano (Alvarado et al. 2006). If this assumption was incorrect, and the temperature was
560 50°C lower (or higher), the timescales obtained from diffusion modeling for diffusion episode 1
561 would be longer (or shorter) by a factor of ~2.4. For diffusion episode 2, we assumed a temperature

of 1080°C, based on olivine-melt thermometry for basaltic andesites erupted from Irazú in 1723 (Benjamin et al. 2007). If this temperature was actually 50°C lower for the samples investigated in our study (basaltic andesites erupted in 1963-65), the timescales obtained from diffusion modeling for diffusion episode 2 would be longer by a factor of ~2.6. As summarized in Costa et al. (2008), at any given temperature the uncertainty of $D_{Fe\text{-}Mg}$ resulting solely from the experimental calibration is a factor of ~2. Incorrect assumptions for the oxygen fugacity prevailing during the diffusion stages may also lead to over- or underestimations of diffusion times (Oeser et al. 2015); however, these are minor compared to those arising from errors of temperatures estimates. For example, if the oxygen fugacity was at $\Delta\log fO_2$ (NNO) = 0 (instead of +1 as presumed in our model) during diffusion episode 1, modeled timescales would be longer by a factor of ~1.5. Given these uncertainties, we are confident that the overall uncertainty of the timescales determined by diffusion modeling in this study is not larger than a factor of 4 which is typical for the calculation of timescales from diffusion modeling in magmatic systems (Costa et al. 2008).

Assembling the Irazú magma prior to the 1963-65 eruption

The new results from Fe-Mg isotopes generally corroborate the timescales of magma transport through the crustal magma system (Ruprecht and Plank 2013). By expanding our analysis to crystals with intermediate Fo, high Ni cores we can provide a more complete picture of the architecture of the magma system beneath Irazú and the assembly of the magma prior to the 1963-65 eruption (Fig. 12). Comparison with other crustal cumulate olivine data from crustal sections (e.g. Otamendi et al. 2016) suggests that the intermediate Fo, high Ni cores are not simple olivine phenocrysts that represent a different magma batch in the crust. Instead, they are best explained as xenocrystic olivine that was picked up by the primitive magma as it intersected an olivine

586 cumulate. The high Ni/Cr ratio in these cores are consistent with this interpretation and suggest that
587 during olivine cumulate formation pyroxenes co-crystallized and through time both mineral phases
588 equilibrated so that Ni was incorporated into the olivine at the expense of pyroxene and Cr behaves
589 in reverse being concentrated in the pyroxenes. Typical distribution coefficients for Cr and Ni
590 between olivine and clinopyroxene are <0.01 and ~4, respectively (Otamendi et al. 2016). The
591 observed concentrations are consistent with this model as Cr content in the xenocrystic cores is one
592 to two orders of magnitude lower than in common olivines and Ni is about a factor of 2 higher.
593 Our model suggests that the primitive magma intersected a mafic (maybe ultramafic) crustal
594 cumulate on its way to the surface. The fact that olivine cores are overgrown by primitive Ni-rich,
595 high Fo mantles further indicates that this contamination of the erupted magma occurred at a depth
596 well below the shallow Irazú magma plumbing system. We have not attempted to estimate the
597 depth for this cumulate, but comparing our results to a crustal section study that exposes olivine
598 cumulates of similar geochemical characteristics within the section suggests at least mid-crustal
599 levels (>15 km depth; Otamendi et al. 2016) and potentially lower crustal conditions. Those
600 depths/pressures are constrained through phase assemblages and compositions studied in this
601 crustal section. Irrespective of the exact location of olivine cumulate contamination, crystal zoning
602 correlations between type A and B olivines provides evidence that the primitive high Fo olivines
603 must originate from greater depth and likely crystallized near the Moho (as it was previously
604 postulated by Ruprecht and Plank, 2013), precluding aphyric magma ascent of primitive melts to
605 shallow levels with ensuing crystallization near the shallow crustal magma reservoirs (Fig. 12).
606

607 **Diffusion of chromium in olivine**

608 The coupling of Fe-Mg isotope and elemental zoning results provide valuable constraints for the
609 growth and diffusion history of the Irazú olivines. As indicated by the Fe-Mg isotopic zoning,

chemical zoning was essentially driven by chemical diffusion following rapid (near instantaneous) growth. This finding allows to utilize Irazú olivines to calculate relative diffusion coefficients for Cr, Al, and V. We focus on Cr, Al, and V diffusivities as those are much less understood than divalent minor and major elements in olivine (Fe-Mg, Mn, Ca, Ni). In particular, Cr and Al diffusivities have been argued to vary over orders of magnitude (Cr: Ito and Ganguly 2006; Spandler and O'Neill 2010; Jollands et al. 2018; Al: Milman-Barris et al. 2008; Spandler and O'Neill 2010; Zhukova et al. 2017). The variations in Cr diffusion have been reconciled recently by Jollands et al. (2018) recognizing that low a_{SiO2} systems (Ito and Ganguly 2006) may show slow Cr diffusion, while high a_{SiO2} systems near the olivine-enstatite buffer (Spandler and O'Neill 2010) lead to significantly faster Cr diffusion. Moreover it was documented that Cr diffusion is strongly concentration dependent (Jollands et al. 2018), an effect that cannot be explored in this study meaningfully.

We do not attempt to estimate specific diffusivities for a specific temperature as we think that there are still significant uncertainties with the analysis of these natural olivines. Neither temperature nor oxygen fugacity in the Irazú magmatic system (thought to be near NNO+1, Benjamin et al. 2007, setting valence states of predominantly Cr^{3+} and V^{4+}, Papike et al. 2005; Mallmann and O'Neill 2009) is tightly constrained when compared to experimental studies. However, as chemical zoning is primarily a result of chemical diffusion and not growth for the investigated olivine crystals, we can determine Cr and, with a higher uncertainty, V and Al diffusion relative to each other and to that of experimentally well-determined Fe-Mg inter-diffusion (Fig. 13).

For this approach to produce meaningful diffusivity estimates, we assume that the zoning profile in the olivines is generated by diffusion following a rapid growth period that generated a step function as starting conditions for diffusion and therefore represents a maximum diffusivity estimate. The previously discussed Fe-Mg isotope zoning supports in general this diffusion-dominated regime for

634 the studied olivines. Secondly, to extract diffusivity information on these elements one has to
635 ensure that the finite (measured) lengthscale of the zoning profiles is primarily a true (diffusion-
636 generated) zoning profile in the crystals and not an artifact of the acquisition method using a
637 scanning laser with a continuous time series. The laser spot size of 25 μm and the continuous
638 sample movement underneath the laser intrinsically creates zonation patterns with a measurable
639 lengthscale, where even true step functions would be smeared to resemble an evolving diffusion
640 profile (Bradshaw and Kent 2017; Fig. S6 in the supplementary material). With increasing
641 diffusion length scale (e.g., due to increasing diffusivity, Fig. S6) zoning profiles acquired during
642 laser ablation and the true zoning profiles converge, and the sampling bias by a continuously
643 moving laser track becomes negligible. To quantitatively compare true zoning and laser-generated
644 profiles we extrapolate the maximum slope at the center where the curvature of the profile changes
645 signs to the concentration plateaus of the step functions and obtain a conservative estimate Δx for
646 the diffusion profile length for all elements of interest (Fig. S7, Tab. S4). Comparing the apparent
647 diffusivity as a function of the lengthscale Δx one can see that as Δx approaches the spot size (25
648 μm) the profile cannot be resolved unambiguously and any calculated diffusivity becomes
649 increasingly overestimated. We can correct for this effect by calculating a smearing factor that
650 accounts for the laser-generated smearing effects. All reported lengthscales Δx for all elements
651 (Tab. S4) are significantly larger than the minimum spatial resolution, thus supporting the notion
652 that these profiles are not simple step functions. As a result we can estimate diffusivities and apply
653 a correction factor for the smearing that varies between 1.399 (Δx = 32 μm) and 1.071 (Δx =
654 71μm). No correction was applied for zoning lengthscales >100 μm as our analysis was limited to
655 Δx < 100 μm and the polynomial approximation is overestimating the smearing effect for large Δx.
656 Lastly, we neglect potential effects of off-perpendicular (relative to the crystal-melt interface)
657 sectioning of the crystals. Imaging of the crystals prior to and after LA-ICP-MS analysis, after

polishing (typically removal of ~10-20 μm) prior to MC-ICP-MS analysis, and again after polishing post MC-ICP-MS analysis shows that zoning evolution into the Z-direction of the crystal is persistent and crystal shapes in general change only to a small degree. This suggests that crystal sectioning was close to perpendicular relative to the crystal-melt interface for most crystals. In summary, the calculated zoning lengthscales and crystal imaging suggest that the profiles represent gradational zoning in Cr content from core to rim and, together with the Fe-Mg isotope zoning record, we can estimate elemental diffusivities for selected elements.

After the smearing correction is applied we find that $D_{Fe\text{-}Mg} > D_V > D_{Cr} > D_{Al}$. Our most robust results − given that we find similar diffusivities for 7 crystals and 9 different traverses (figures 13, 14 and S8) − are for D_{Cr} , which is smaller than $D_{Fe\text{-}Mg}$ by a factor of 4.9 ± 2.9, with the uncertainty representing 1SD (standard deviation) of the calculated population of diffusion coefficients. Therefore, the results from these natural olivines are consistent with fast Cr diffusion under high a_{SiO2} conditions (Spandler and O'Neill 2010; Jollands et al. 2018). Al and V are less well constrained, because zoning profiles are not consistently correlated with Fo content and, in the case of Al, our analytical uncertainties were high relative to Cr concentrations in all of our IZ-10-13 olivines. Nonetheless, the two olivine crystals for which Al zoning was distinct suggest that Al diffusivity may still be faster than inferred from other studies (Milman-Barris et al. 2008; Spandler and O'Neill 2010) consistent with results for Al diffusion in olivine under high a_{SiO2} (Zhukova et al. 2017). A more extensive analysis will be required in the future, especially given that the comparison (Fig. 13) with data from Spandler and O'Neill (2010) is done at different temperatures. While our diffusivity ratios are calculated for a temperature of about ~1150˚C, Spandler and O'Neill (2010) ran their experiments at 1300˚C. Thus, potential differences in the activation energy (~ 200 kJ/(mol K) for Fe-Mg inter-diffusion in olivine, Dohmen et al. 2007; >300 kJ/(mol K) for Cr in olivine, Ito and Ganguly 2006, Jollands et al. 2018) are not accounted for in this comparison.

682 The lower activation energy for Fe-Mg inter-diffusion suggests that $D_{Fe\text{-}Mg}/D_{Cr}$ should increase
683 with lower temperatures as Cr diffusion is slowed more effectively at low T. Lastly, V diffusivity,
684 as determined by the zoning profiles of only four olivine crystals (Fig. 13 and 14), is smaller than
685 $D_{Fe\text{-}Mg}$ by a factor of 2.5 ± 1.4. However, the activation energy for V diffusion is not known and an
686 analysis for different temperatures cannot be performed. Given that V will not only be present as
687 tetravalent species in terrestrial magmas, but also to some degree trivalent (Papike et al. 2005;
688 Mallmann and O'Neill 2009) it will require more experimental work to fully characterize V
689 diffusion in olivine under common oxygen fugacities.
690 These results for diffusivities in olivine of selected tri- and tetravalent cations are, with the
691 exception of Al, in good agreement with those of the previous study of Spandler and O'Neill
692 (2010) who also did not provide diffusivities for a range of temperatures, but rather limited their
693 experimental investigation to 1300 ˚C using San Carlos olivine (Fig. 13). In the latter study the
694 authors had excellent crystallographic control and provided diffusivity estimates for all three
695 crystallographic orientations and all their diffusivities are of similar order of magnitude to
696 diffusivities from this study. The olivines in this study experienced lower temperatures (<1200 ˚C,
697 see Ruprecht and Plank 2013, for additional discussion on this) compared to that of the
698 experimental study of Spandler and O'Neill (2010). Both studies utilized natural olivines, and the
699 San Carlos olivines as well as the overgrowth mantles in the Irazú olivines have high Fo contents
700 of ~ Fo90. However, given the limitations of our analysis, the determined diffusivities represent
701 maximum diffusivity estimates and while they overlap with experimental results (Spandler and
702 O'Neill 2010; Jollands et al. 2018) this agreement may break down if any made assumption is not
703 maintained. The result would be smaller diffusivities. Given the good agreement however and the
704 fact that a_{SiO2} (e.g., Jollands et al. 2018) is a likely factor controlling the differences in diffusivities
705 suggest that our analysis is robust. Nonetheless, additional similar studies on natural samples,

706 together with experimental studies, may enable to elucidate reasons for a range in diffusivity for
707 specific elements.
708
709
710 **Implications**
711 The findings of this study demonstrate that a combination of Fe-Mg chemical and isotopic profiles
712 in complexly zoned olivines provides reliable information on the origin of zoning and thus, enables
713 to unravel complex crystal growth and diffusion histories. This information can be used to optimize
714 diffusion modeling in order to estimate the time scales of magmatic processes. In the case of
715 olivines from Irazú volcano, such diffusion modeling yields the time span for the transfer of
716 material from the middle or lower crust to the shallow plumbing system (<300 days for 6 out of 7
717 olivine crystals), but also magma mixing-to-eruption timescales. These are in good agreement with
718 the timescales of ascent of mantle-derived magmas, as determined by diffusion modeling of Ni
719 zoning in primitive olivines (Ruprecht and Plank 2013). Mixing-to-eruption times for crustal
720 olivines beneath the continental arc volcano Irazú appear to be short (<600 days in most cases) −
721 despite a magma storage region in the shallow crust − and thus imply that material from the lower
722 or middle crust can be transported to the shallow plumbing system and eventually to the vent of an
723 arc volcano while the eruption is already underway.
724 Xenocrystic olivines may provide independent constraints on the diffusivity of commonly slow-
725 diffusing elements such as Cr and Al for which the determination of diffusivities by experimental
726 approaches is challenging. However, analysis of Irazú olivines with xenocrystic cores and Cr
727 zoning suggests that under those natural conditions Cr diffusion in olivine may be faster than
728 previously determined by experiments. Additional studies are required to fully understand the
729 mechanisms of Cr diffusion and whether elevated trace impurities and defects or the chemical

activity of major elements are causing the enhanced diffusivity, as suggested for other elements and in olivine and other phases (e.g. Zhukova et al. 2014; Ferriss et al. 2016; Jollands et al. 2018).

Acknowledgements

This study was supported by the project funding program "Wege in die Forschung II" of the Leibniz Universität Hannover. P.R. acknowledges support from the U.S. National Science Foundation (EAR 1426820/1719687). We are grateful to M. Jollands and C. Sio for very constructive reviews and we thank R. Almeev for efficient editorial handling.

References

Alvarado, G.E., Carr, M.J., Turrin, B.D., Swisher, C.C., Schmincke, H.-U., and Hudnut, K.W. (2006) Recent volcanic history of Irazú volcano, Costa Rica: Alternation and mixing of two magma batches, and pervasive mixing. Geological Society of America Special Papers , 412, 259–276.

Benjamin, E.R., Plank, T., Wade, J.A., Kelley, K.A., Hauri, E.H., and Alvarado, G.E. (2007) High water contents in basaltic magmas from Irazú Volcano, Costa Rica. Journal of Volcanology and Geothermal Research, 168, 68–92.

Bradshaw, R.W., and Kent, A.J.R. (2017) The analytical limits of modeling short diffusion timescales. Chemical Geology, 466, 667–677.

Carr, M.J. (1984) Symmetrical and Segmented Variation of Physical and Geochemical Characteristics of the Central American Volcanic Front. Journal of Volcanology and

754 Geothermal Research, 20, 231–252.
755 Chakraborty, S. (1997) Rates and mechanisms of Fe-Mg interdiffusion in olivine at 980°–1300°C.
756 Journal of Geophysical Research, 102, 12317–12331.
757 Chakraborty, S. (2010) Diffusion Coefficients in Olivine, Wadsleyite and Ringwoodite. Reviews in
758 Mineralogy and Geochemistry, 72, 603–639.
759 Collinet, M., Charlier, B., Namur, O., Oeser, M., Médard, E., and Weyer, S. (2017) Crystallization
760 history of enriched shergottites from Fe and Mg isotope fractionation in olivine megacrysts.
761 Geochimica et Cosmochimica Acta, 207, 277–297.
762 Costa, F., and Chakraborty, S. (2004) Decadal time gaps between mafic intrusion and silicic
763 eruption obtained from chemical zoning patterns in olivine. Earth and Planetary Science
764 Letters, 227, 517–530.
765 Costa, F., and Dungan, M. (2005) Short time scales of magmatic assimilation from diffusion
766 modeling of multiple elements in olivine. Geology, 33, 837–840.
767 Costa, F., Dohmen, R., and Chakraborty, S. (2008) Time Scales of Magmatic Processes from
768 Modeling the Zoning Patterns of Crystals. Reviews in Mineralogy and Geochemistry, 69,
769 545–594.
770 Crank, J. (1975) The Mathematics of Diffusion, second edi., 421 p. Clarendon Press, Oxford.
771 Dohmen, R., and Chakraborty, S. (2007) Fe-Mg diffusion in olivine II: Point defect chemistry,
772 change of diffusion mechanisms and a model for calculation of coefficients in natural olivine.
773 Physics and Chemistry of Minerals, 34, 409–430.
774 Donaldson, C.H. (1975) Calculated diffusion coefficients and the growth rate of olivine in a basalt
775 magma. Lithos, 8, 163–174.
776 Dzierma, Y., Thorwart, M.M., Rabbel, W., Flueh, E.R., Alvarado, G.E., and Mora, M.M. (2010)
777 Imaging crustal structure in south central Costa Rica with receiver functions. Geochemistry,

778 Geophysics, Geosystems, 11, 1–21.
779 Ferriss, E., Plank, T., and Walker, D. (2016) Site-specific hydrogen diffusion rates during
780 clinopyroxene dehydration. Contributions to Mineralogy and Petrology, 171, 1–24.
781 Gazel, E., Hayes, J.L., Hoernle, K., Kelemen, P., Everson, E., Holbrook, W.S., Hauff, F., van den
782 Bogaard, P., Vance, E.A., Chu, S., and others (2015) Continental crust generated in oceanic
783 arcs. Nature Geoscience, 8, 321–327.
784 Global Volcanism Program (2013) Irazu (345060). In E. Venzke, Ed., Volcanoes of the World.
785 Smithsonian Institution. http://volcano.si.edu/volcano.cfm?vn=345060
786 Hartley, M.E., Morgan, D.J., Maclennan, J., Edmonds, M., and Thordarson, T. (2016) Tracking
787 timescales of short-term precursors to large basaltic fissure eruptions through Fe–Mg
788 diffusion in olivine. Earth and Planetary Science Letters, 439, 58–70.
789 Hier-Majumder, S., Anderson, I.M., and Kohlstedt, D.L. (2005) Influence of protons on Fe-Mg
790 interdiffusion in olivine. Journal of Geophysical Research B: Solid Earth, 110, 1–12.
791 Ito, M., and Ganguly, J. (2006) Diffusion kinetics of Cr in olivine and 53Mn–53Cr
792 thermochronology of early solar system objects. Geochimica et Cosmochimica Acta, 70, 799–
793 809.
794 Jambon, A., Lussiez, P., Clocchiatti, R., Weisz, J., and Hernandez, J. (1992) Olivine growth rates
795 in a tholeiitic basalt: An experimental study of melt inclusions in plagioclase. Chemical
796 Geology, 96, 277–287.
797 Jarosewich, E., Nelen, J.A., and Norberg, J.A. (1980) Reference Samples for Electron Microprobe
798 Analysis. Geostandards Newsletter, 4, 43–47.
799 Jollands, M., Hermann, J., O'Neill, H.S.C., Spandler, C., and Padrón-Navarta, J.A. (2016a)
800 Diffusion of Ti and some Divalent Cations in Olivine as a Function of Temperature, Oxygen
801 Fugacity, Chemical Potentials and Crystal Orientation. Journal of Petrology, 57, 1983–2010.

Jollands, M.C., O'Neill, H.S.C., and Hermann, J. (2014) The importance of defining chemical potentials, substitution mechanisms and solubility in trace element diffusion studies: the case of Zr and Hf in olivine. Contributions to Mineralogy and Petrology, 168, 1055.

Jollands, M.C., Burnham, A.D., O'Neill, H.S.C., Hermann, J., and Qian, Q. (2016b) Beryllium diffusion in olivine: A new tool to investigate timescales of magmatic processes. Earth and Planetary Science Letters, 450, 71–82.

Jollands, M.C., O'Neill, H.S.C., Van Orman, J., Berry, A.J., Hermann, J., Newville, M., and Lanzirotti, A. (2018) Substitution and diffusion of Cr2+ and Cr3+ in synthetic forsterite and natural olivine at 1200–1500 °C and 1 bar. Geochimica et Cosmochimica Acta, 220, 407–428.

Kahl, M., Chakraborty, S., Costa, F., and Pompilio, M. (2011) Dynamic plumbing system beneath volcanoes revealed by kinetic modeling, and the connection to monitoring data: An example from Mt. Etna. Earth and Planetary Science Letters, 308, 11–22.

Kahl, M., Chakraborty, S., Costa, F., Pompilio, M., Liuzzo, M., and Viccaro, M. (2013) Compositionally zoned crystals and real-time degassing data reveal changes in magma transfer dynamics during the 2006 summit eruptive episodes of Mt. Etna. Bulletin of Volcanology, 75, 1–14.

Kahl, M., Chakraborty, S., Pompilio, M., and Costa, F. (2015) Constraints on the Nature and Evolution of the Magma Plumbing System of Mt. Etna Volcano (1991–2008) from a Combined Thermodynamic and Kinetic Modelling of the Compositional Record of Minerals. Journal of Petrology, 56, 2025–2068.

Lazarov, M., and Horn, I. (2015) Matrix and energy effects during in-situ determination of Cu isotope ratios by ultraviolet-femtosecond laser ablation multicollector inductively coupled plasma mass spectrometry. Spectrochimica Acta Part B: Atomic Spectroscopy, 111, 64–73.

Lizarralde, D., Holbrook, W.S., Van Avendonk, H.J., Mora Fernandez, M., Alvarado, G.E., and

826 Harder, S.H. (2010) Crustal structure along the active Costa Rican volcanic arc. In AGU Fall
827 Meeting Abstracts p. T13A–2176.
828 Longpré, M.-A., Klügel, A., Diehl, A., and Stix, J. (2014) Mixing in mantle magma reservoirs prior
829 to and during the 2011-2012 eruption at El Hierro, Canary Islands. Geology, 42, 315–318.
830 Maaløe, S. (2011) Olivine phenocryst growth in Hawaiian tholeiites: Evidence for supercooling.
831 Journal of Petrology, 52, 1579–1589.
832 Mallmann, G., O'Neill, H.S.C., and Klemme, S. (2009) Heterogeneous distribution of phosphorus
833 in olivine from otherwise well-equilibrated spinel peridotite xenoliths and its implications for
834 the mantle geochemistry of lithium. Contributions to Mineralogy and Petrology, 158, 485–
835 504.
836 Milman-Barris, M.S., Beckett, J.R., Baker, M.B., Hofmann, A.E., Morgan, Z., Crowley, M.R.,
837 Vielzeuf, D., and Stolper, E. (2008) Zoning of phosphorus in igneous olivine. Contributions to
838 Mineralogy and Petrology, 155, 739–765.
839 Oeser, M., Weyer, S., Horn, I., and Schuth, S. (2014) High-Precision Fe and Mg Isotope Ratios of
840 Silicate Reference Glasses Determined In Situ by Femtosecond LA-MC-ICP-MS and by
841 Solution Nebulisation MC-ICP-MS. Geostandards and Geoanalytical Research, 38, 311–328.
842 Oeser, M., Dohmen, R., Horn, I., Schuth, S., and Weyer, S. (2015) Processes and time scales of
843 magmatic evolution as revealed by Fe–Mg chemical and isotopic zoning in natural olivines.
844 Geochimica et Cosmochimica Acta, 154, 130–150.
845 Otamendi, J.E., Tiepolo, M., Walker, B.A., Cristofolini, E.A., and Tibaldi, A.M. (2016) Trace
846 elements in minerals from mafic and ultramafic cumulates of the central Sierra de Valle Fértil,
847 Famatinian arc, Argentina. Lithos, 240–243, 355–370.
848 Papike, J.J., Karner, J.M., and Shearer, C.K. (2005) Comparative planetary mineralogy: Valence
849 state partitioning of Cr, Fe, Ti, and V among crystallographic sites in olivine, pyroxene, and

spinel from planetary basalts. American Mineralogist, 90, 277–290.

Qian, Q., O'Neill, H.S.C., and Hermann, J. (2010) Comparative diffusion coefficients of major and trace elements in olivine at 950 C from a xenocryst included in dioritic magma. Geology, 38, 331–334.

Rae, A.S.P., Edmonds, M., Maclennan, J., Morgan, D., Houghton, B., Hartley, M.E., and Sides, I. (2016) Time scales of magma transport and mixing at Kilauea Volcano, Hawai'i. Geology, 44, 463–466.

Richter, F., Chaussidon, M., Mendybaev, R., and Kite, E. (2016) Reassessing the cooling rate and geologic setting of Martian meteorites MIL 03346 and NWA 817. Geochimica et Cosmochimica Acta, 182, 1–23.

Richter, F.M., Liang, Y., and Davis, A.M. (1999) Isotope fractionation by diffusion in molten oxides. Geochimica et Cosmochimica Acta, 63, 2853–2861.

Richter, F.M., Davis, A.M., DePaolo, D.J., and Watson, E.B. (2003) Isotope fractionation by chemical diffusion between molten basalt and rhyolite. Geochimica et Cosmochimica Acta, 67, 3905–3923.

Rubin, A.M. (1995) Propagation of Magma-Filled Cracks. Annual Review of Earth and Planetary Sciences, 23, 287–336.

Ruprecht, P., and Plank, T. (2013) Feeding andesitic eruptions with a high-speed connection from the mantle. Nature, 500, 68–72.

Ruprecht, P., Bergantz, G.W., and Dufek, J. (2008) Modeling of gas-driven magmatic overturn: Tracking of phenocryst dispersal and gathering during magma mixing. Geochemistry Geophysics Geosystems, 9, 1–20.

Schleicher, J.M., and Bergantz, G.W. (2017) The Mechanics and Temporal Evolution of an Open-system Magmatic Intrusion into a Crystal-rich Magma. Journal of Petrology, 58, 1059–1072.

874 Schwab, R.G., and Küstner, D. (1981) The equilibrium fugacities of important oxygen buffers in
875 technology and petrology. Neues Jahrbuch für Mineralogie-Abhandlungen, 140, 111–142.
876 Shea, T., Lynn, K.J., and Garcia, M.O. (2015) Cracking the olivine zoning code: Distinguishing
877 between crystal growth and diffusion. Geology, 43, 935–938.
878 Sio, C.K.I., and Dauphas, N. (2017) Thermal and crystallization histories of magmatic bodies by
879 Monte Carlo inversion of Mg-Fe isotopic profiles in olivine. Geology, 44, G38056.1.
880 Sio, C.K.I., Dauphas, N., Teng, F.-Z., Chaussidon, M., Helz, R.T., and Roskosz, M. (2013)
881 Discerning crystal growth from diffusion profiles in zoned olivine by in situ Mg–Fe isotopic
882 analyses. Geochimica et Cosmochimica Acta, 123, 302–321.
883 Spandler, C., and O'Neill, H.S.C. (2010) Diffusion and partition coefficients of minor and trace
884 elements in San Carlos olivine at 1,300°C with some geochemical implications. Contributions
885 to Mineralogy and Petrology, 159, 791–818.
886 Spandler, C., O'Neill, H.S.C., and Kamenetsky, V.S. (2007) Survival times of anomalous melt
887 inclusions from element diffusion in olivine and chromite. Nature, 447, 303–6.
888 Teng, F.-Z., Dauphas, N., Helz, R.T., Gao, S., and Huang, S. (2011) Diffusion-driven magnesium
889 and iron isotope fractionation in Hawaiian olivine. Earth and Planetary Science Letters, 308,
890 317–324.
891 Tollan, P.M.E., O'Neill, H.S.C., Hermann, J., Benedictus, A., and Arculus, R.J. (2015) Frozen
892 melt-rock reaction in a peridotite xenolith from sub-arc mantle recorded by diffusion of trace
893 elements and water in olivine. Earth and Planetary Science Letters, 422, 169–181.
894 Van Orman, J.A., and Krawczynski, M.J. (2015) Theoretical constraints on the isotope effect for
895 diffusion in minerals. Geochimica et Cosmochimica Acta, 164, 365–381.
896 Wang, Z., Hiraga, T., and Kohlstedt, D.L. (2004) Effect of H+ on Fe-Mg interdiffusion in olivine,
897 (Fe,Mg)2SiO4. Applied Physics Letters, 85, 209–211.

Watson, E.B., Cherniak, D.J., and Holycross, M.E. (2015) Diffusion of phosphorus in olivine and molten basalt. American Mineralogist, 100, 2053–2065.

White, R.W. (1966) Ultramafic inclusions in basaltic rocks from Hawaii. Contributions to Mineralogy and Petrology, 12, 245–314.

Zhukova, I., O'Neill, H.S.C., Cambell, I.H., and Kilburn, M.R. (2014) The effect of silica activity on the diffusion of Ni and Co in olivine. Contributions to Mineralogy and Petrology, 168, 1029.

Zhukova, I., O'Neill, H., and Campbell, I.H. (2017) A subsidiary fast-diffusing substitution mechanism of Al in forsterite investigated using diffusion experiments under controlled thermodynamic conditions. Contributions to Mineralogy and Petrology, 172, 1–12.

Figure Captions

Figure 1. Schematic architecture of Irazú magma system (modified from Ruprecht and Plank 2013) and the origin of distinct olivine types A-C. Green represents primitive magnesian olivines (Fo_{89-91}), or the Mg-rich rims (Fo_{87-90}) grown around crystal cores with intermediate Fo contents (Fo_{80-87}; blue) when the latter were picked up by ascending mantle melts. Orange represents normally zoned (Fo_{87-90} to Fo_{79-84}) outer rims of olivine crystals or intermediate to low Fo olivines from the shallow magma storage region.

Figure 2. BSE and reflected-light images of two olivine crystals investigated in this study. (**a**) and (**c**) BSE images of crystals IZ-10-12 ol16 and IZ-10-12 ol11, respectively, before in-situ analyses of Fe-Mg isotopic profiles by LA-MC-ICP-MS. (**b**) and (**d**) Reflected-light images of the same crystals after the in-situ analyses by LA-MC-ICP-MS.

Figure 3. Examples of type A (**left**) and type B (**right**) olivine crystals from Irazú. Type A olivines show reverse Ni zoning at constant and high Fo and Cr contents in their cores, while type B olivines display reverse zoning of Fo and Cr (and in some cases also of Al and V) as well as very low Cr concentrations in their cores..

Figure 4. Ni/Cr versus Fo content in olivines investigated in this study. Type B olivines are characterized by large Ni/Cr ratios, while type A olivines are constrained to low Ni/Cr ratios at high Fo content. All core-to-rim data for Type B crystals are labeled as xenocrysts and therefore xenocryst rims plot at low Ni/Cr ratios.

Figure 5. Fe-Mg chemical (expressed as Fo) and isotopic profiles for four complexly zoned olivines analyzed in this study. All olivines show strong coupling of Fe-Mg chemical and isotopic zoning (especially for Fe isotopes), indicating equilibration by Fe-Mg inter-diffusion. Sample material of these four olivine crystals was ablated by line scans parallel to the chemical zoning. Error bars represent the analytical uncertainty (2 SD) during one analytical session.

Figure 6. Fe-Mg chemical (expressed as Fo) and isotopic profiles for three primitive, normally zoned olivines investigated in this study. The normal zoning at the rim is strongly coupled with inversely correlated Fe-Mg isotopic profiles, implying diffusive re-equilibration prior to eruption.

945 Sample material of olivine IZ-10-13 ol22 was ablated by line scans perpendicular to the chemical
946 zoning. Error bars represent the analytical uncertainty (2 SD) during one analytical session.
947
948 **Figure 7.** δ^{56}Fe and δ^{26}Mg values for all Fe-Mg isotopic profiles acquired in this study, illustrating
949 that Fe isotope variations (up to 1.7‰) are much more pronounced than Mg isotope variations
950 (<0.6‰) in all investigated olivine grains.
951
952 **Figure 8.** Results of the stepwise diffusion modeling approach used in this study for a complexly
953 zoned olivine (IZ-10-12 ol16). Profile of Fo contents is based on the calibrated BSE (grayscale)
954 image of this crystal. (**left**) Subfigures show the measured and modeled Fo contents (**a**) and the
955 measured and modeled Fe isotopic compositions (**b**) for diffusion episode 1, assuming a model of
956 instantaneous growth of a Mg-rich layer (distance 0-106 μm in a) and subsequent Fe-Mg inter-
957 diffusion. For diffusion episode 2 (**right**), the diffusion profiles generated during the first diffusion
958 episode are used as the initial concentration (and isotopic) gradients, and only the rim composition
959 (at distance = 0 μm) is modified to simulate diffusion of Fe into (and Mg out of) the olivine.
960
961 **Figure 9.** Results of the stepwise diffusion modeling approach used in this study for a complexly
962 zoned olivine (IZ-10-13 ol34), assuming a model of instantaneous growth of a Mg-rich layer
963 (distance 0-156 μm in a) and subsequent Fe-Mg inter-diffusion for diffusion episode 1 (**left**). This
964 example also illustrates that the second diffusion episode (**right**) with diffusion of Fe into (and Mg
965 out of) the olivine is needed to reproduce the low Fo content (**c**) and relative enrichment of light Fe
966 isotopes (**d**) near the rim. Note that the profile of Fo contents is shown as measured by EMPA. For
967 further details, see figure caption of Fig. 8.
968

969 **Figure 10.** Comparison of modeling results obtained from two models for diffusion episode 1
970 (instantaneous growth and subsequent diffusion [**left**] vs. growth and simultaneous diffusion
971 [**right**]), both of which are followed by simple diffusive Fe-Mg exchange between crystal and melt
972 (diffusion episode 2, lasting 448 days in this case). Both models for diffusion episode 1 are able to
973 reproduce the Fe-Mg chemical (**a, c**) and Fe isotopic zoning (**b, d**) of this olivine reasonably well.
974
975 **Figure 11.** Comparison of modeling results obtained from two models for diffusion episode 1
976 (instantaneous growth and subsequent diffusion [**left**] vs. growth and simultaneous diffusion
977 [**right**]), both of which are followed by simple diffusive Fe-Mg exchange between crystal and melt
978 (diffusion episode 2, lasting 11 days in this case). Both models for diffusion episode 1 are able to
979 reproduce the Fe-Mg chemical zoning of this olivine (**a, c**); however, the second model yields a
980 much better fit to the Fe isotopic zoning of this crystal (**d**), indicating that the shorter diffusion
981 timescale (110+11 days) is more likely in this case.
982
983 **Figure 12.** Schematic architecture of Irazú magma system (modified from Ruprecht and Plank
984 2013) with information about major and trace element characteristics of the three main olivine
985 types and about timescales of transport (Δt) as deduced in this study from diffusion modeling at the
986 given temperature range (1080-1150°C). Transport timescale for primitive magnesian olivines
987 (green) from MOHO depth is from Ruprecht and Plank (2013), based on diffusion modeling of
988 reverse Ni zoning.
989
990 **Figure 13.** Comparison of Cr, Al, and V diffusivity relative to Fe-Mg inter-diffusion. Filled and
991 open squares are results for smearing corrected and uncorrected profiles, respectively. Al data is
992 limited to sample IZ-10-12, which was measured on a day with better instrument sensitivity. The

993 results for Cr and V diffusivity determined by Spandler and O'Neill (2010; SPO'N10) are shown
994 for comparison, whereas Al diffusion was not quantified in that study. Experiments on Cr
995 diffusion by Jollands et al. (2018) did not explore co-existing Fe-Mg inter-diffusion and therefore
996 no diffusivity ratios are shown for this study. The results from our study are not plotted for specific
997 crystallographic axis, because of random orientations of the diffusion profiles; see supplementary
998 data (Table S3) for rotation angles. Diffusivities were determined by 1D diffusion profiles (see
999 Figure 14).
1000
1001 **Figure 14.** LA-ICPMS rim-to-center analyses for Fo and Al (white squares) as well as Cr and V
1002 (gray squares). Calculated diffusion profiles used for the relative determination of elemental
1003 diffusivities are shown as black (Fo, Al) and gray (Cr, V) lines. Profiles were calculated separately
1004 for each element with a step profile. Step location was chosen to minimize misfit for the respective
1005 element. Near-rim zoning is ignored as it probably includes effects of fractional crystallization.
1006 Additional Fo, V, and Cr zoning profiles are shown in the supplementary material (Fig. S8).
1007
1008

This is a preprint, the final version is subject to change, of the American Mineralogist (MSA)
Cite as Authors (Year) Title. American Mineralogist, in press.
DOI: https://doi.org/10.2138/am-2018-6258

Figure 1

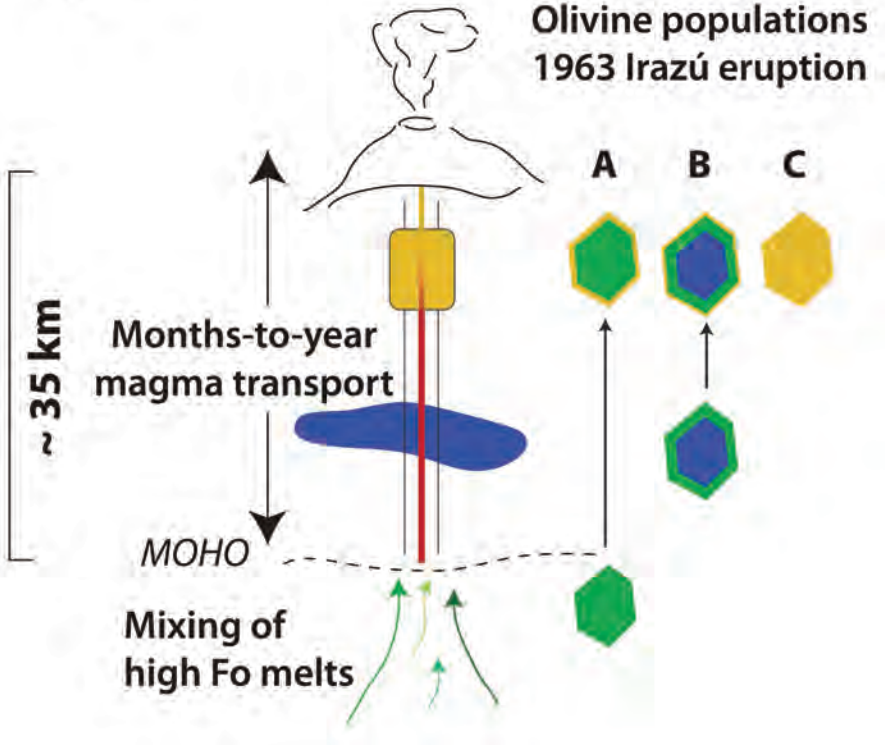

Figure 2

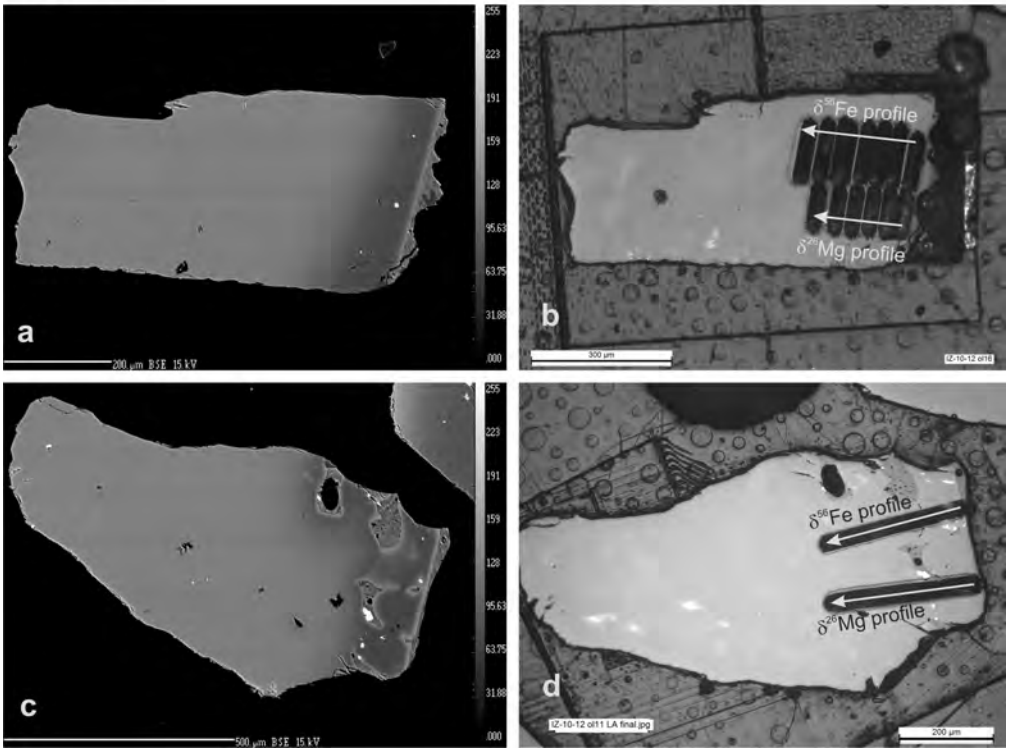
a
200 µm BSE 15 kV
255
223
191
159
128
95.63
63.75
31.88
.000
b
δ56Fe profile
δ26Mg profile
300 µm
IZ-10-12 oil6
c
500 µm BSE 15 kV
d
δ56Fe profile
δ26Mg profile
IZ-10-12 oil11 LA final.jpg
200 µm

Figure 3

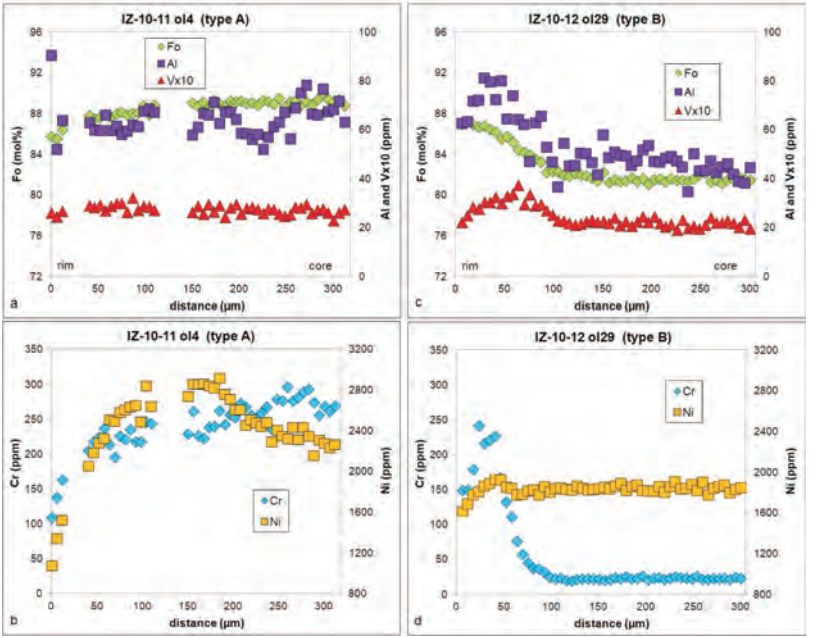
IZ-10-11 ol4 (type A)
Fo
Al
Vx10
Fo (mol%)
Al and Vx10 (ppm)
rim
core
distance (μm)
a
IZ-10-12 ol29 (type B)
Fo
Al
Vx10
Fo (mol%)
Al and Vx10 (ppm)
rim
core
distance (μm)
c
IZ-10-11 ol4 (type A)
Cr
Ni
Cr (ppm)
Ni (ppm)
distance (μm)
b
IZ-10-12 ol29 (type B)
Cr
Ni
Cr (ppm)
Ni (ppm)
distance (μm)
d

Figure 4

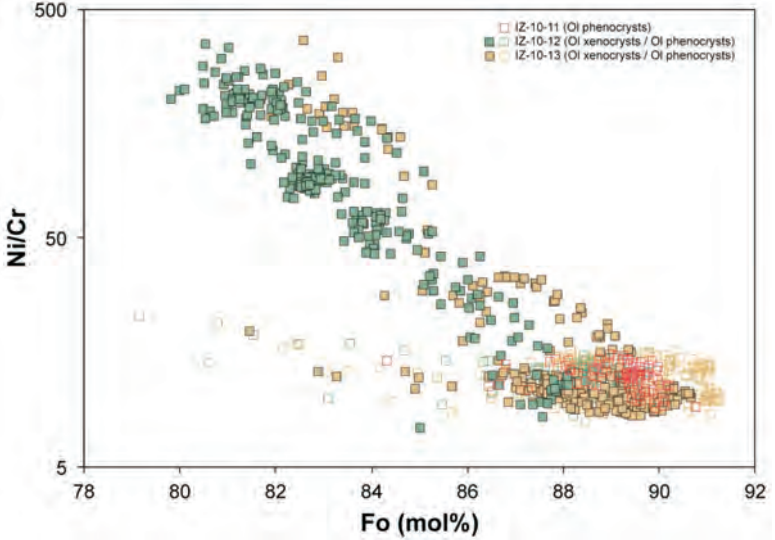
IZ-10-11 (Ol phenocrysts)
IZ-10-12 (Ol xenocrysts / Ol phenocrysts)
IZ-10-13 (Ol xenocrysts / Ol phenocrysts)
500
50
5
Ni/Cr
78
80
82
84
86
88
90
92
Fo (mol%)

Figure 5

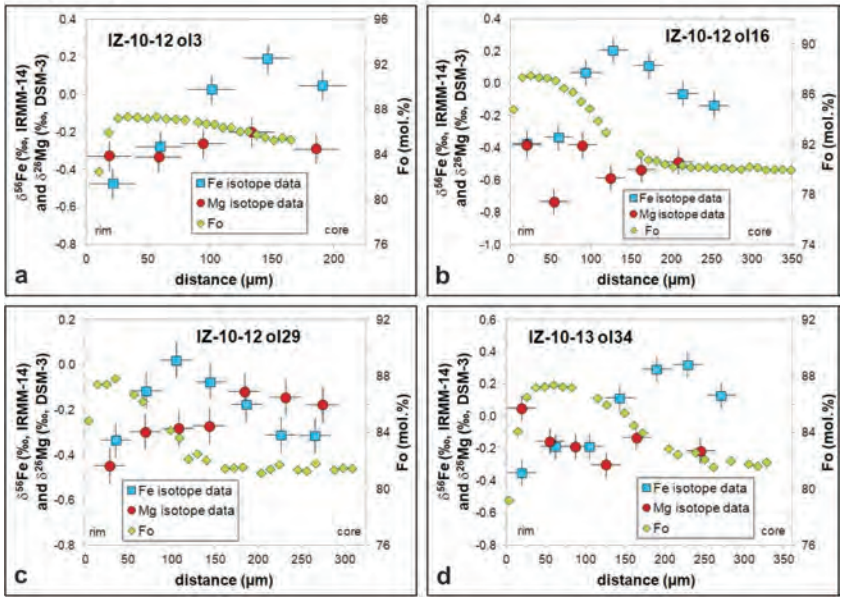
IZ-10-12 ol3
IZ-10-12 ol16
IZ-10-12 ol29
IZ-10-13 ol34
δ56Fe (‰, IRMM-14) and δ26Mg (‰, DSM-3)
Fo (mol.%)
distance (μm)
Fe isotope data
Mg isotope data
Fo
rim
core
a
b
c
d

Figure 6

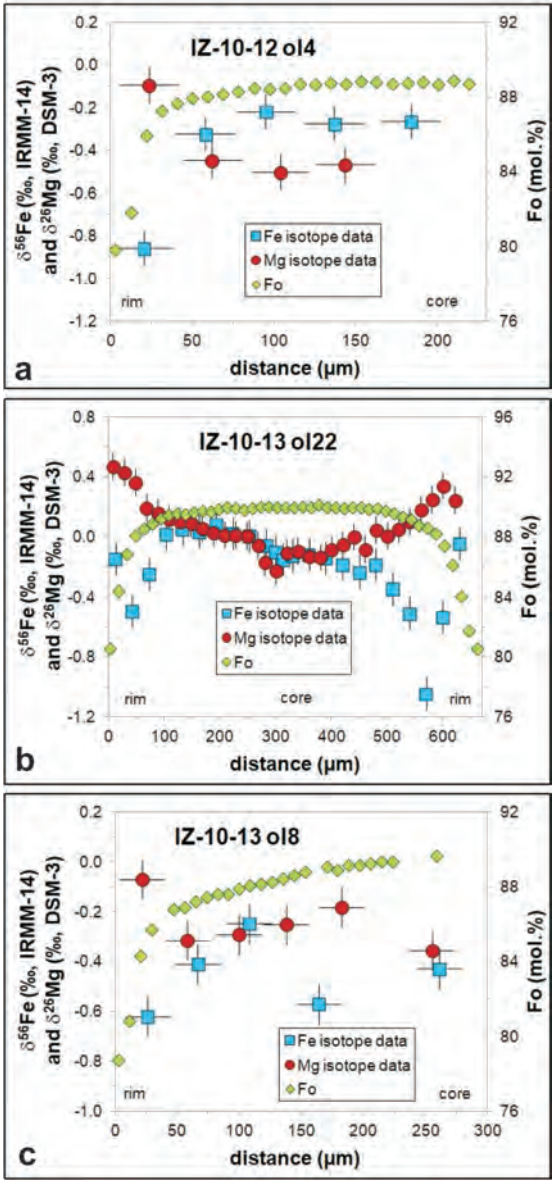
IZ-10-12 ol4
δ56Fe (‰, IRMM-14) and δ26Mg (‰, DSM-3)
Fo (mol.%)
Fe isotope data
Mg isotope data
Fo
rim
core
distance (µm)
a
IZ-10-13 ol22
rim
core
rim
b
IZ-10-13 ol8
c

Figure 7

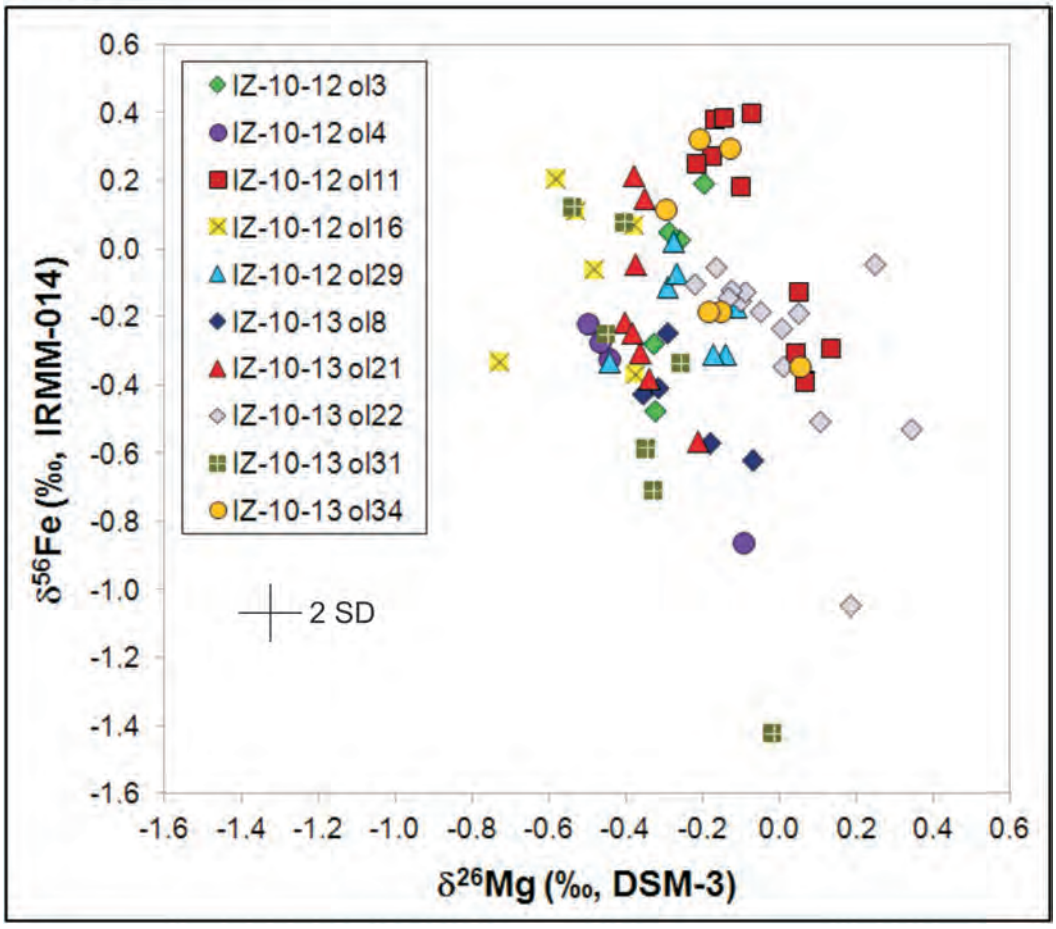
IZ-10-12 ol3
IZ-10-12 ol4
IZ-10-12 ol11
IZ-10-12 ol16
IZ-10-12 ol29
IZ-10-13 ol8
IZ-10-13 ol21
IZ-10-13 ol22
IZ-10-13 ol31
IZ-10-13 ol34
2 SD
δ56Fe (‰, IRMM-014)
δ26Mg (‰, DSM-3)
0.6
0.4
0.2
0.0
-0.2
-0.4
-0.6
-0.8
-1.0
-1.2
-1.4
-1.6
-1.6 -1.4 -1.2 -1.0 -0.8 -0.6 -0.4 -0.2 0.0 0.2 0.4 0.6

Figure 8

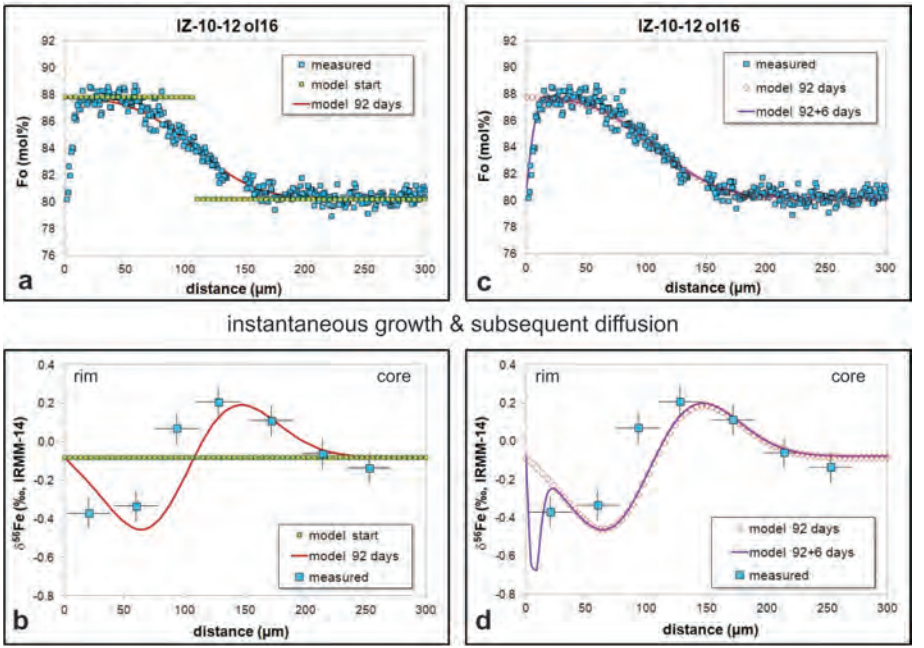
IZ-10-12 ol16
Fo (mol%)
distance (µm)
measured
model start
model 92 days
a
IZ-10-12 ol16
Fo (mol%)
distance (µm)
measured
model 92 days
model 92+6 days
c
instantaneous growth & subsequent diffusion
rim
core
δ56Fe (‰, IRMM-14)
distance (µm)
model start
model 92 days
measured
b
rim
core
δ56Fe (‰, IRMM-14)
distance (µm)
model 92 days
model 92+6 days
measured
d

Figure 9

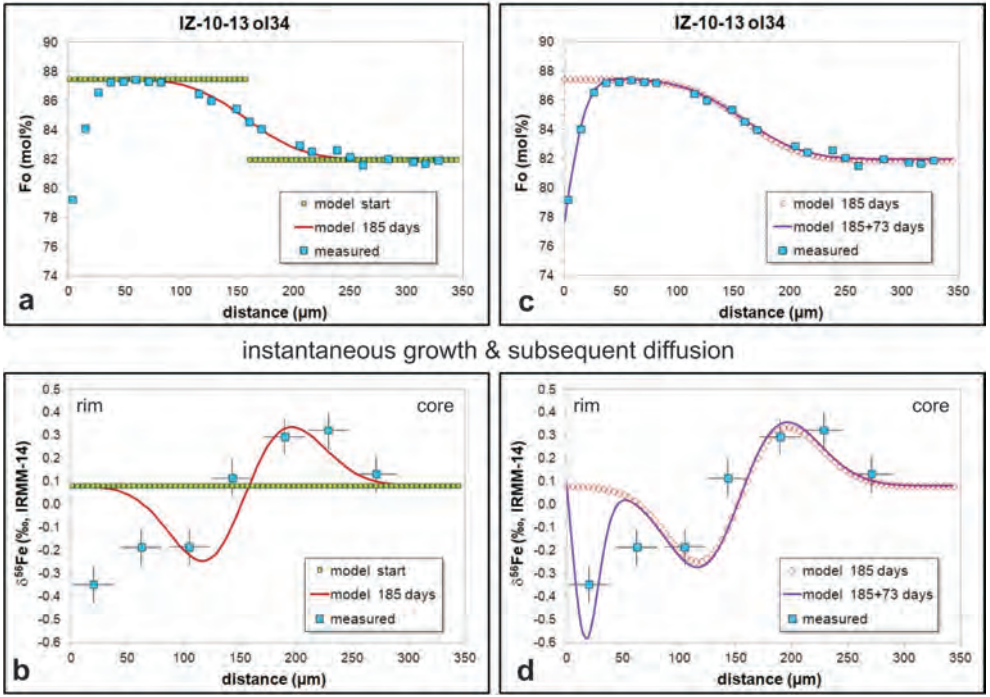
IZ-10-13 ol34
Fo (mol%)
distance (µm)
model start
model 185 days
measured
a
IZ-10-13 ol34
Fo (mol%)
distance (µm)
model 185 days
model 185+73 days
measured
c
instantaneous growth & subsequent diffusion
rim
core
δ56Fe (‰, IRMM-14)
distance (µm)
model start
model 185 days
measured
b
rim
core
δ56Fe (‰, IRMM-14)
distance (µm)
model 185 days
model 185+73 days
measured
d

Figure 10

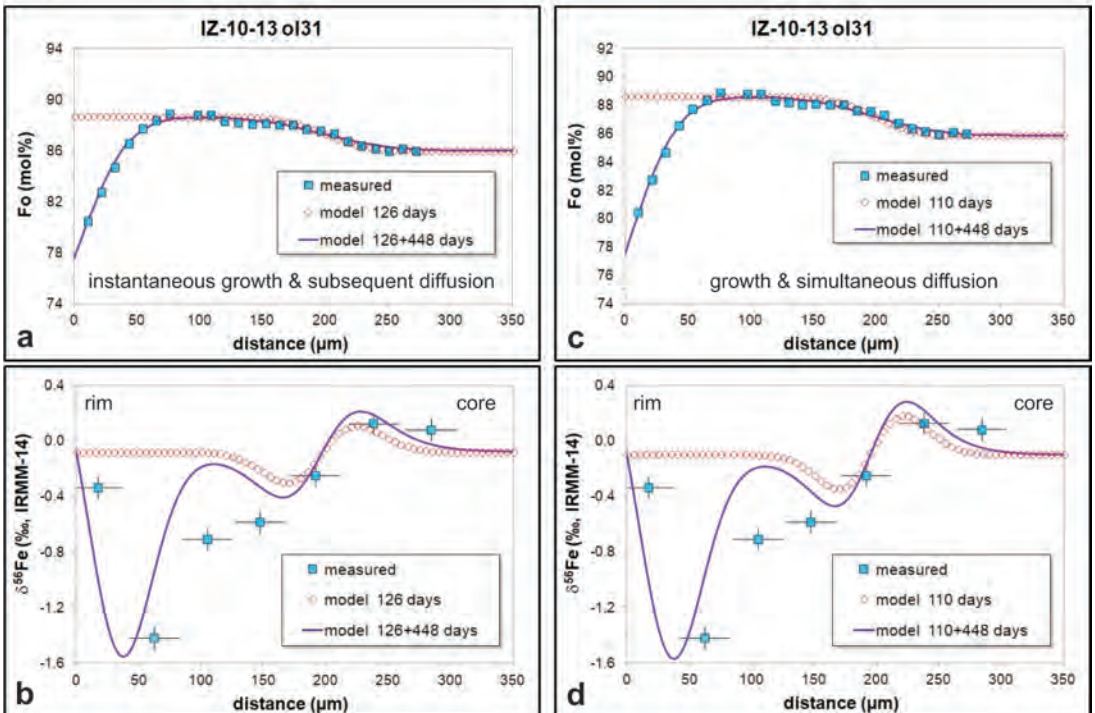
IZ-10-13 ol31
Fo (mol%)
measured
model 126 days
model 126+448 days
instantaneous growth & subsequent diffusion
distance (µm)
a
IZ-10-13 ol31
Fo (mol%)
measured
model 110 days
model 110+448 days
growth & simultaneous diffusion
distance (µm)
c
rim
core
δ56Fe (‰, IRMM-14)
measured
model 126 days
model 126+448 days
distance (µm)
b
rim
core
δ56Fe (‰, IRMM-14)
measured
model 110 days
model 110+448 days
distance (µm)
d

Figure 11

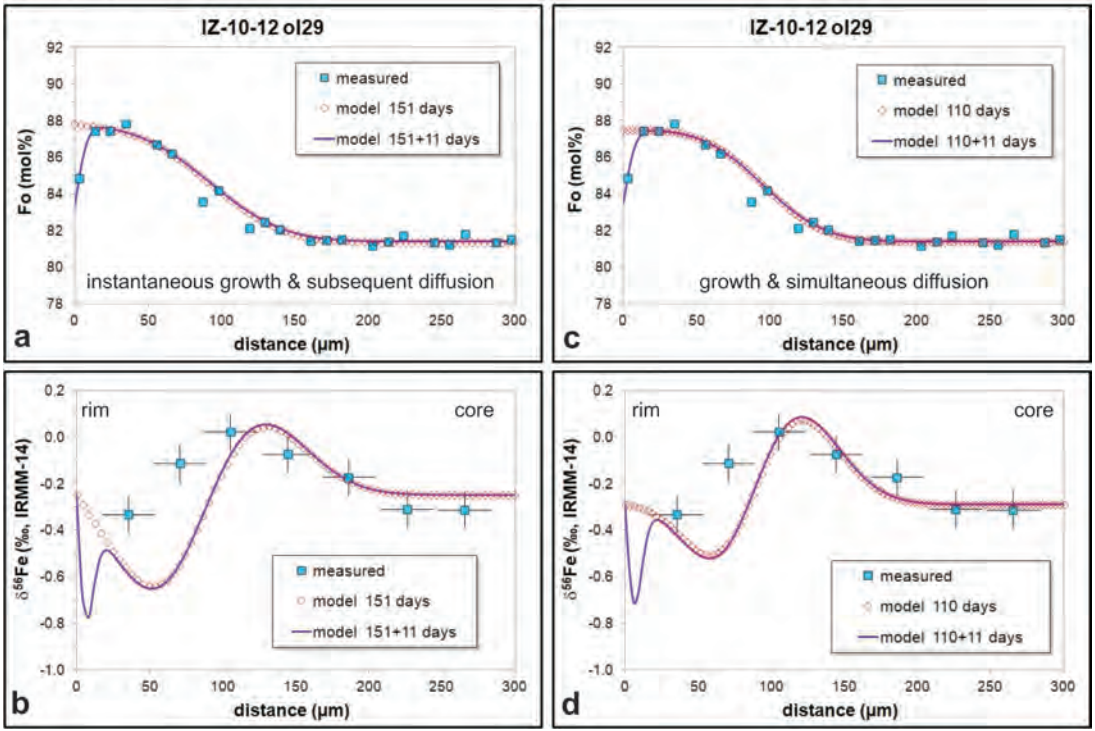
IZ-10-12 ol29
Fo (mol%)
measured
model 151 days
model 151+11 days
instantaneous growth & subsequent diffusion
distance (µm)
a
IZ-10-12 ol29
Fo (mol%)
measured
model 110 days
model 110+11 days
growth & simultaneous diffusion
distance (µm)
c
rim
core
δ56Fe (‰, IRMM-14)
measured
model 151 days
model 151+11 days
distance (µm)
b
rim
core
δ56Fe (‰, IRMM-14)
measured
model 110 days
model 110+11 days
distance (µm)
d

Figure 12

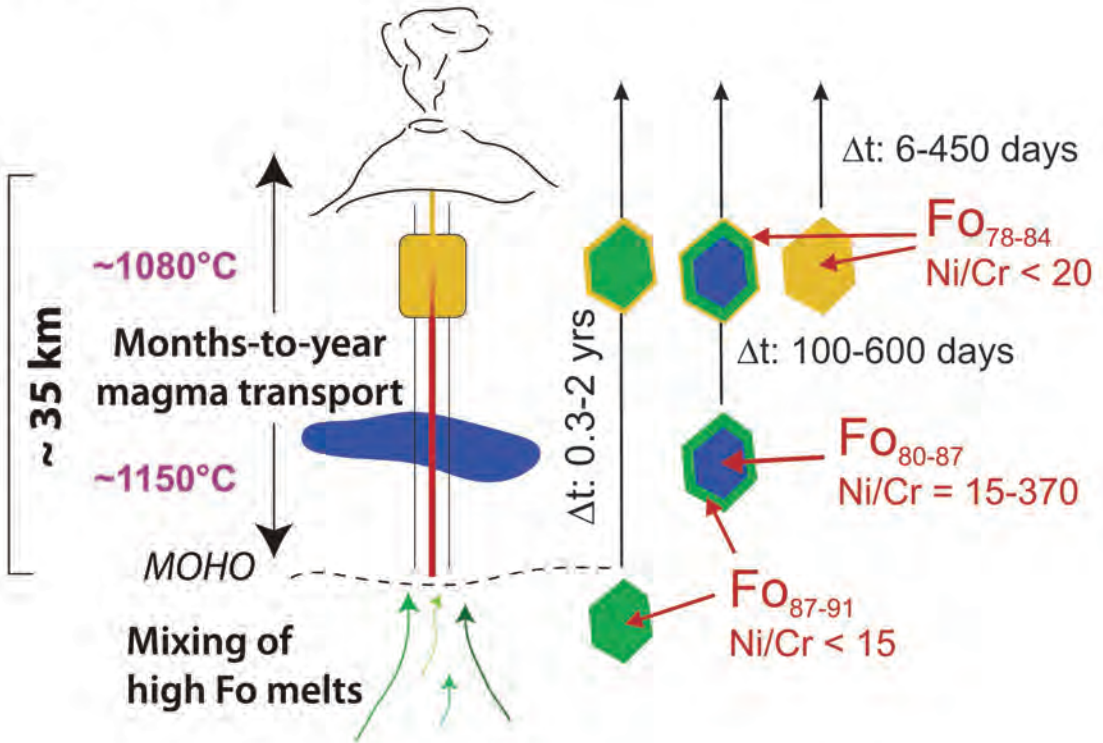
~ 35 km
~1080°C
Months-to-year
magma transport
~1150°C
MOHO
Mixing of
high Fo melts
Δt: 0.3-2 yrs
Δt: 6-450 days
Fo78-84
Ni/Cr < 20
Δt: 100-600 days
Fo80-87
Ni/Cr = 15-370
Fo87-91
Ni/Cr < 15

Figure 13

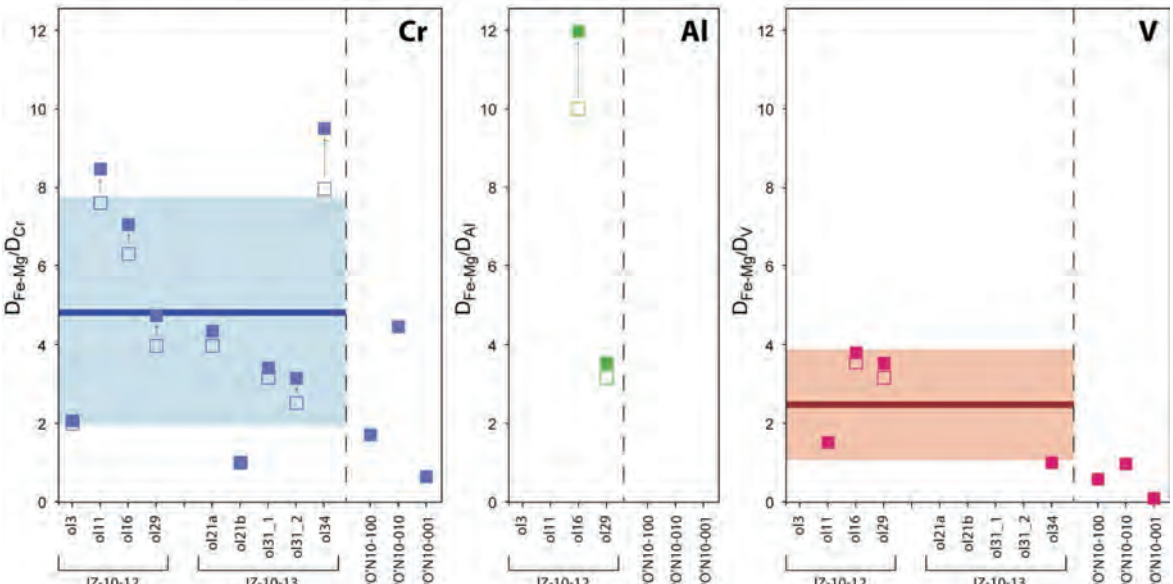
Cr
Al
V
$D_{Fe\text{-}Mg}/D_{Cr}$
$D_{Fe\text{-}Mg}/D_{Al}$
$D_{Fe\text{-}Mg}/D_{V}$
0
2
4
6
8
10
12
ol3
ol11
ol16
ol29
ol21a
ol21b
ol31_1
ol31_2
ol34
SPO'N10-100
SPO'N10-010
SPO'N10-001
IZ-10-12
IZ-10-13

Figure 14

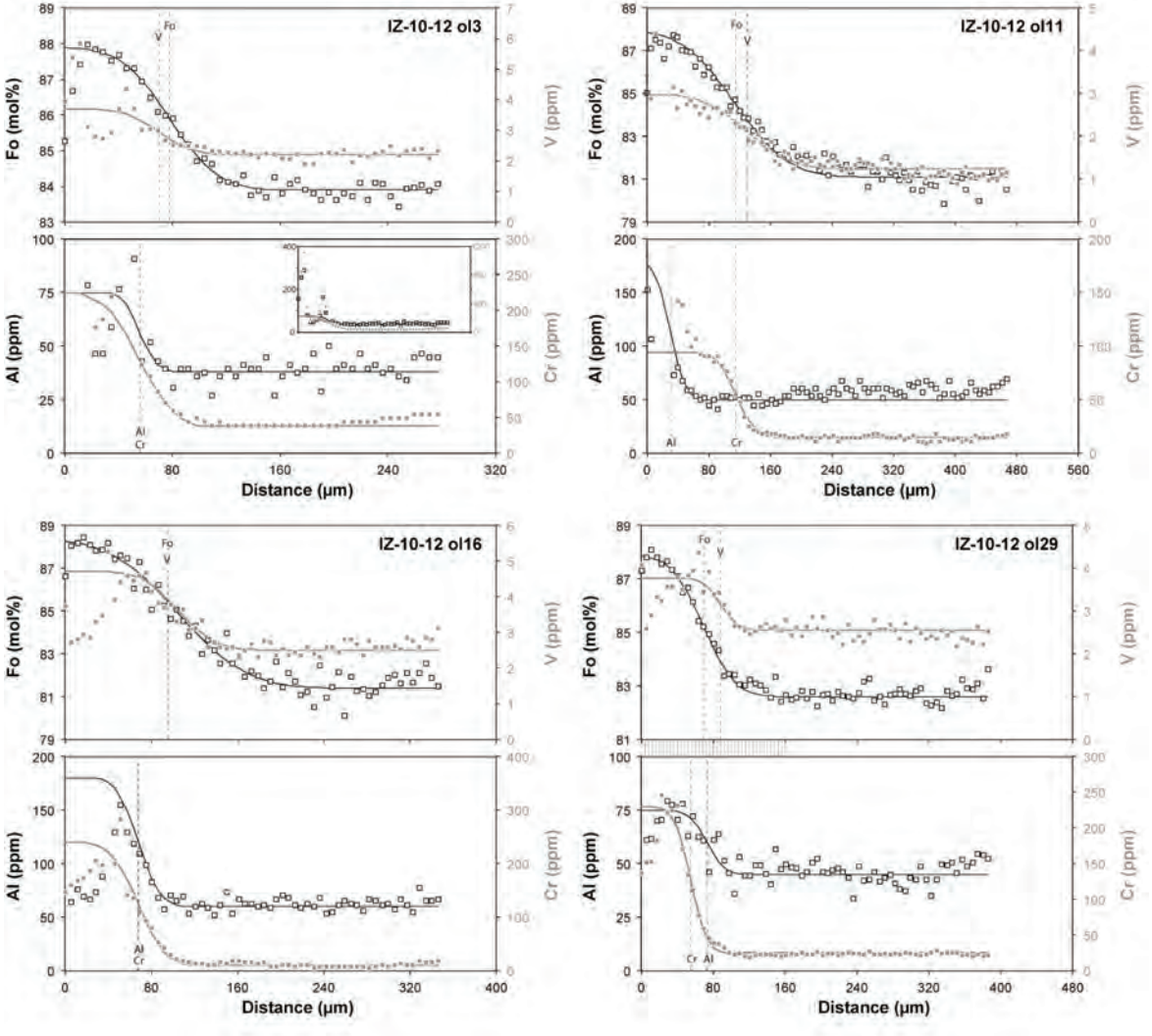
IZ-10-12 ol3
IZ-10-12 ol11
IZ-10-12 ol16
IZ-10-12 ol29
Fo (mol%)
V (ppm)
Al (ppm)
Cr (ppm)
Distance (μm)
Fo
V
Al
Cr

Table 1: Timescales of diffusive re-equilibration for complexly and normall

sample	type of Fe-Mg zoning	t1 (days) [a]	t2 (days) [b]	t_{total} (days) [c]
IZ-10-12 ol3	complex	168	48	216
IZ-10-12 ol11	complex	533 [d]	56 [d]	589
IZ-10-12 ol16	complex	92	6	98
IZ-10-12 ol29	complex	151	11	162
IZ-10-13 ol21	complex	294	1456	1750
IZ-10-13 ol31	complex	126	448	574
IZ-10-13 ol34	complex	185	73	258
IZ-10-12 ol4	normal	x [e]	168	168
IZ-10-13 ol8	(multiple) normal	x	112	112
IZ-10-13 ol22	normal	x	224	224

[a] Model parameters for diffusion episode 1: T = 1150°C, fO_2 at NNO+1, X_{Fe} = 0.15, P =

[b] Model parameters for diffusion episode 2: T = 1080°C, fO_2 at NNO+1, X_{Fe} = 0.15, P =

[c] Given the uncertainties of the temperature estimation (±50°C), of the assumed fO_2, an

[d] Timescales obtained by fitting the width of the isotopic diffusion profile, as the Fe-Mg c

[e] x = not applicable.

y zoned Irazú olivines, using a model of instantaneous growth and subsequent diffu

β_{Fe}	$\cos(\alpha)^2$	$\cos(\beta)^2$	$\cos(\gamma)^2$
0.205	0.952	0.009	0.038
0.220	0.900	0.086	0.014
0.150	0.324	0.140	0.535
0.180	0.045	0.755	0.200
0.250	0.261	0.733	0.006
0.220	0.638	0.313	0.050
0.160	0.576	0.281	0.142
0.120	0.514	0.436	0.050
0.150	0.735	0.215	0.051
0.140	0.016	0.012	0.972

= 500 MPa.

= 100 MPa.

d of the experimental calibration of $D_{Fe\text{-}Mg}$, the uncertainty of the modeled timescales is whithin a f

hemical diffusion profile appears to be distorted due to the polishing of the crystal before the EMPA

sion for diffusion episode 1 (t1) if applicable.

actor of 4.

Table 2: Timescales of diffusive re-equilibration and integrated growth rat

sample	type of Fe-Mg zoning	t1 (days) [a]	t2 (days) [b]	t_{total} (days)
IZ-10-12 ol3	complex	128	48	176
IZ-10-12 ol11	complex	530 [d]	56 [d]	586
IZ-10-12 ol16	complex	90	6	96
IZ-10-12 ol29	complex	110	11	121
IZ-10-13 ol21	complex	290	1456	1746
IZ-10-13 ol31	complex	110	448	558
IZ-10-13 ol34	complex	180	73	253

[a] Model parameters for diffusion episode 1: T = 1150°C, fO_2 at NNO+1, X_{Fe} = 0.15, P

[b] Model parameters for diffusion episode 2: T = 1080°C, fO_2 at NNO+1, X_{Fe} = 0.15, P

[c] Rate of growth (R) of the Mg-rich layer during diffusion episode 1.

[d] Timescales obtained by fitting the width of the isotopic diffusion profile, as the Fe-Mg

[e] Peclet number ($R \cdot \Delta x / D$), where R is the growth rate, Δx is the zoning lenghtscale, ar

:es for complexly zoned Irazú olivines, using a model of growth and simultaneo

growth rate (m/s) [c]	Pe [e]
1.0×10^{-11}	21
3.0×10^{-12}	13
1.3×10^{-11}	16
9.5×10^{-12}	12
1.0×10^{-11}	38
2.1×10^{-11}	46
9.9×10^{-12}	22

= 500 MPa.

= 100 MPa.

chemical diffusion profile appears to be distorted due to the polishing of the crystal before th

ıd D is the diffusion coefficient, for diffusion episode 1.

ɔus diffusion for diffusion episode 1 (t1).

e EMPA.